1 **Sensitivity of meteorological forcing resolution on hydrologic variables**

3 Fadji Z. Maina[1*], Erica R. Siirila-Woodburn[1], Pouya Vahmani[2]

6 [1] Energy Geosciences Division, Lawrence Berkeley National Laboratory 1 Cyclotron Road, M.S.

7 74R-316C, Berkeley, CA 94704, USA

8 [2] Climate and Ecosystem Sciences Division, Lawrence Berkeley National Laboratory 1

9 Cyclotron Road, M.S. 74R-316C, Berkeley, CA 94704, USA

11 *Corresponding Author: fadjimaina@lbl.gov

14    **Abstract**
15
16    Projecting the spatio-temporal changes in water resources under a no-analog future climate

17    requires physically-based integrated hydrologic models, which simulate the transfer of water and

18    energy across the earth's surface. These models show promise in the context of unprecedented

19    climate extremes given their reliance on the underlying physics of the system as opposed to

20    empirical relationships. However, these techniques are plagued by several sources of uncertainty,

21    including the inaccuracy of input datasets such as meteorological forcing. These datasets, usually

22    derived from climate models or satellite-based products, are typically only resolved on the order

23    of tens to hundreds of kilometers, while hydrologic variables of interest (e.g. discharge,

24    groundwater levels) require a resolution at much smaller scales. In this work, a high-resolution

25    hydrologic model is forced with various resolutions of meteorological forcing (0.5 to 40.5 km)

26    generated by a dynamical downscaling analysis from the regional climate model Weather

27    Research and Forecasting (WRF). The Cosumnes watershed, which spans the Sierra Nevada and

28    Central Valley interface of California (USA), exhibits semi-natural flow conditions due to its

29    rare un-dammed river basin and is used here as a testbed to illustrate potential impacts of various

30    resolutions of meteorological forcing on snow accumulation and snowmelt, surface runoff,

31    infiltration, evapotranspiration, and groundwater levels. Results show that the errors in spatial

32    distribution patterns impact land surface processes and can be delayed in time. Localized biases

33    in groundwater levels can be as large as 5-10 m, and 3 m in surface water. Most hydrologic

34    variables reveal that biases are seasonally and spatially-dependent, which can have serious

35    implications for model calibration and ultimately water management decisions.

## 1. Introduction

Understanding water and energy fluxes across the Earth's critical zone, a region spanning from bedrock to vegetation canopy, is important to assess the impacts of climate change on water resources. Integrated hydrologic models, solving water-energy interactions and transfers, across the lower-atmosphere, the land surface, and the subsurface, allow to analyze water resources in both time and space and to project into a no-analog future where empirical models are no longer valid. With the advancement of computing power, these high-fidelity, high-resolution models are becoming widely used (e.g. MIKE-SHE (Abbott et al., 1986), HydroGeoSphere (Panday and Huyakorn, 2004), and ParFlow-CLM (Maxwell and Miller, 2005)). However, their implementation can be plagued by several sources of uncertainty. While the accuracy, the precision, and the uncertainty reduction of hydrologic models are extensively discussed in the literature, more attention is given to the physical representation of the phenomena occurring in the hydrological systems (Beven, 1993; Beven and Binley, 1992; Liu and Gupta, 2007), the reduction of uncertainties related to the hydrodynamic parameters (Gilbert et al., 2016; Janetti et al., 2019; Maina and Guadagnini, 2018; Srivastava et al., 2014), and the numerical resolution of the mathematical equations governing the physics of the environment (Belfort et al., 2009; Bergamaschi and Putti, n.d.; Fahs et al., 2009; Hassane Maina and Ackerer, 2017; Miller et al., 1998; Tocci et al., 1997).

Atmospheric dynamics (e.g. precipitation patterns) constitute one of the main drivers of the simulated hydrologic processes. Unfortunately, measuring atmospheric conditions is difficult, and is often only at point locations with stations which are difficult to maintain. Thus, models relying on data assimilation methods that fuse observations at different scales and remote sensing

59    products are commonly used to generate the spatiotemporal distribution of meteorological

60    variables. Furthermore, because integrated hydrologic models require many meteorological

61    variables (i.e. precipitation, temperature, wind speed, solar radiation, air pressure, and relative

62    humidity), synthetic data from climate models are often used due to the scarcity of

63    measurements. In addition, in the context of climate change, only climate models can provide a

64    spatial distribution of future meteorological conditions. Also, integrated hydrologic models

65    require high resolution forcing to ensure fidelity and accuracy and meteorological variables such

66    as precipitation, one of the most important data and key control of hydrological models, are very

67    heterogeneous especially in mountainous areas (Olsson et al., 2014; Prein et al., 2013).

68       Like any model input, meteororological forcing is impacted by several sources of

69    uncertainty, including the fidelity of the physics of the atmospheric model as well as the

70    representativity of the spatial resolution at which they occur. The impact of precipitation

71    resolution on runoff and streamflow is widely documented in the literature with studies relying

72    on *(i)* empirical hydrologic models with precipitation data coming from measurements (Arnaud

73    et al., 2002; Berne et al., 2004; Lobligeois et al., 2014; Nicótina et al., 2008; Schilling, 1991;

74    Shrestha et al., 2006; Tobin et al., 2011), satellite-based products (Koren et al., 1999; Ochoa-

75    Rodriguez et al., 2015; Vergara et al., 2013) and climate models outputs (Dankers et al., 2007;

76    Kleinn et al., 2005) and *(ii)* physics-based hydrologic models with precipitation data coming

77    from measurements (Elsner et al., 2014; Fu et al., 2011), satellite-based products (Eum et al.,

78    2014; Haddeland et al., 2006) and climate models outputs (Mendoza et al., 2016; Rasmussen et

79    al., 2011). Moreover, Rasmussen et al., (2011) study the impact of meteorological forcing on

80    snow dynamics.

81    Nevertheless, previous studies were mostly focused on runoff and streamflow analysis,

82    lacking a complete analysis of all the hydrodynamic processes occurring at the watershed scale.

83    Moreover, the resolutions of the meteorological data (~km) used remain relatively coarse

84    compared to the scale of resolution of the hydrological models (~m). Hence, the objective of this

85    study is to investigate the impact of the spatial resolution of the meteorological forcing from

86    ~km to ~m on the hydrologic processes occurring at the watershed scale using a physics-based

87    integrated hydrologic model. In other words, we seek to understand how the uncertainties

88    associated with the coarse spatial resolution of meteorological forcing propagate into the high-

89    resolution integrated hydrologic models and affect the output of interest.

90    While in this study we utilize specific models to quantify the impact of meteorological

91    forcing on hydrologic variables, the results generalized for watershed processes and are meant to

92    be illustrative of the potential bias with various codes and in various locations. In this work, we

93    use ParFlow-CLM (Kollet and Maxwell, 2006; Maxwell, 2013; Maxwell and Miller, 2005)

94    forced with the Weather Research and Forecasting (WRF) model (Skamarock et al., 2008a;

95    Skamarock and Klemp, 2008). ParFlow simulates subsurface and surface flows (as well as their

96    interaction) by solving the mixed form of the Richards equation (Richards, 1931) and the

97    kinematic wave equation, respectively. The transfer of water and energy from the subsurface and

98    the land surface to the atmosphere is simulated using a coupled version of the Community Land

99    Model (CLM, Dai et al., 2003) to ParFlow. Therefore, the model allows for the spatio-temporal

100   analysis of all the hydrological components of interest such as the distribution of pressure-head

101   which encompasses the information on the water level in the river and the groundwater, the

102   groundwater and surface water storages, the evapotranspiration, the infiltration, and the snow

103   dynamics. WRF is a state-of-the-art, fully compressible, non-hydrostatic, mesoscale numerical

104 weather prediction model that simulates the physics governing the atmospheric dynamics using a

105 nested domain configuration to provide meteorological forcing data at different spatial

106 resolutions for ParFlow-CLM.

107 Our study focuses on the Cosumnes watershed located in Northern California, USA, a

108 region where the effects of climate change have already been observed. The latter are

109 characterized by a fluctuation between extreme droughts (Griffin and Anchukaitis, 2014) and the

110 subsequent occurrence of unprecedented wildfires and periods of intense precipitation mainly

111 caused by atmospheric rivers (Dettinger, 2011). Atmospheric rivers, filaments of concentrated

112 moisture in the atmosphere, generate storms with intensity much higher than the average

113 precipitation events and are sometimes very localized. The Cosumnes hosts one of the last rivers

114 without a dam in California, offering the opportunity to study natural flow. The watershed also

115 spans the Sierra Nevada - Central Valley interface, offering an opportunity to assess the

116 relationship between snowpack dynamics, large-scale river runoff, and aquifer storage. The

117 region is representative of many watersheds in the state, given the strong variations in

118 topography and land cover and land use, but also the snow dynamics given that the majority of

119 the water resources in the state originate from snowmelt (Dettinger and Anderson, 2015). These

120 sharp variations in above and below ground heterogeneities necessitate high-resolution models,

121 making it an excellent candidate to understand the impact of the forcing resolution on hydrology.

122 We study the water year 2017, the wettest water year on California record characterized

123 by several atmospheric rivers (Di Liberto, 2017; SCRIPPS Institution of Oceanography, 2017).

124 As mentioned by Swain et al., (2018), the future climate of California will likely be characterized

125 by extreme wet and dry conditions. It is therefore important to understand the dynamics of these

126 currently end-member conditions. Although exceptional today, these extremes will likely

127  become the "new normal" in the future. Wet conditions are also ideal to conservatively

128  understand the amount of bias an overly coarse meteorological forcing dataset might have on a

129  region's hydrology. The developed integrated hydrologic model has a spatial resolution of 200 m

130  and we use five different spatial resolutions (40.5, 13.5, 4.5, 1.5 and 0.5 km) of meteorological

131  forcing derived from the WRF dynamical downscaling approach. Our study aims to answer the

132  following questions:

133  • What is the effect of meteorological forcing spatial resolution on simulated snow

134  accumulation and melt, evapotranspiration, infiltration and pressure head and/or

135  water table depth? In broader terms, how do meteorological uncertainties

136  propagate into the resolved hydrodynamics and which processes require high-

137  resolution meteorological forcing?

138  • At which spatial resolution should the climate models be solved to accurately

139  describe the strong variations in meteorological conditions induced by

140  atmospheric rivers and their effect on the hydrology and therefore water supply?

141

142  **2.  The Cosumnes watershed model**

143      **a.  Study area**

144  The Cosumnes watershed is approximately 7,000 $km^2$ in size (Figure 1a) and hosts one of

145  the last rivers in the region without a major dam. Thus, it offers a rare opportunity to study the

146  natural flow conditions. The geologic composition consists of materials ranging from nearly

147  impermeable formations (volcanic and plutonic rocks located mainly in the Sierra Nevada

148  mountains) to highly porous and permeable aquifers in the Central Valley. The agricultural

149  region of Central Valley, subject to seasonal pumping and irrigation, is located in the southwest

150    of the watershed and consists of various crop types, including alfalfa, pasture lands, and

151    vineyards. The Sierra Nevada Mountains are predominately covered by an evergreen forest.

152    Spatial patterns of precipitation are highly heterogeneous across the watershed. On average, the

153    Sierra Nevada Mountains receive three times more precipitation (1500 mm) than the Central

154    Valley (Cosgrove et al., 2003), primarily in the form of snow. The regional climate is considered

155    Mediterranean, with wet and cold winters (with a watershed average temperature equal to 0 °C)

156    and hot and dry summers (with watershed average temperature reaching  25 °C) (Cosgrove et al.,

157    2003).

158
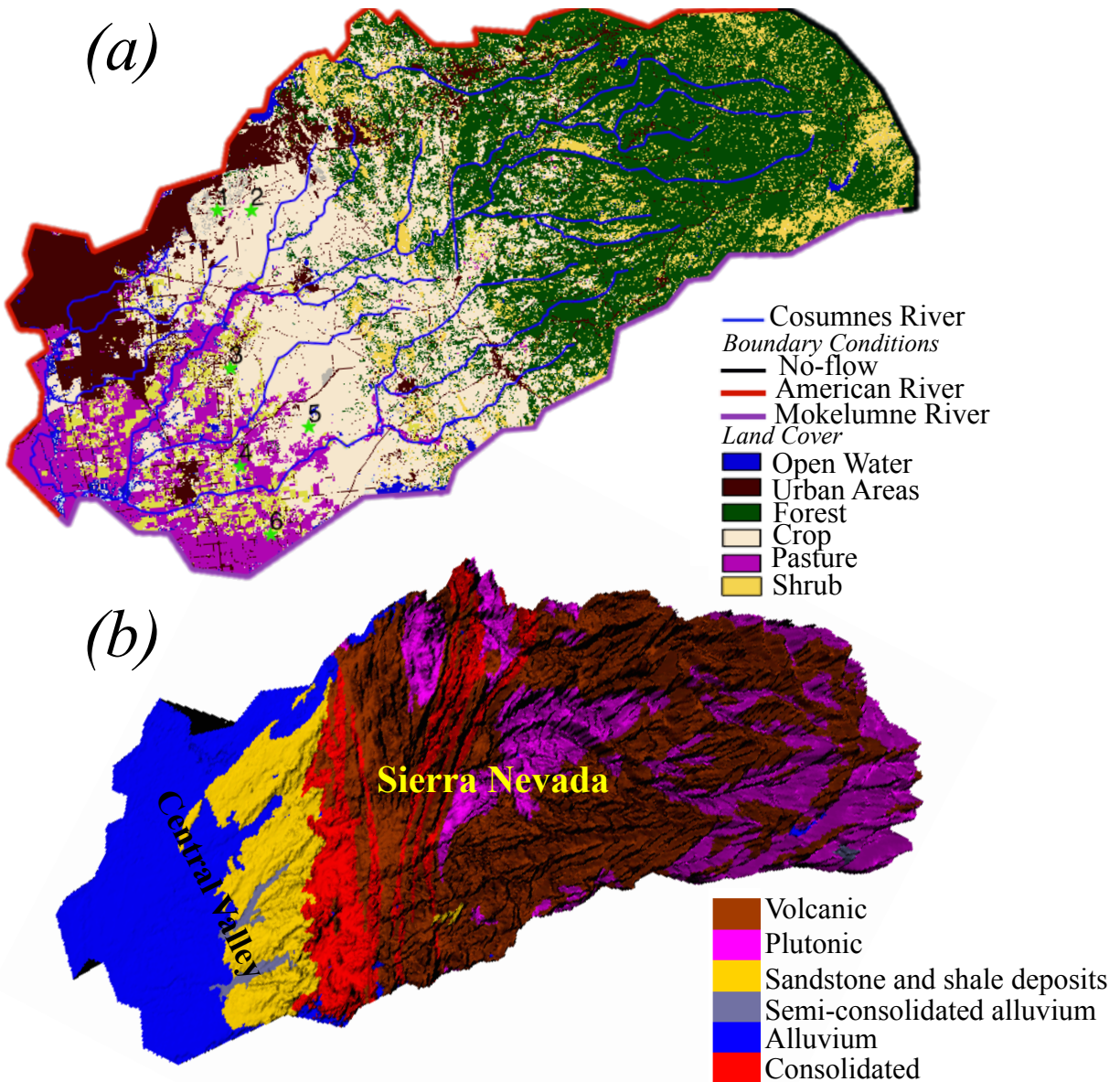
Figure 1: *(a)* Land-use and land-cover (Homer et al., 2015) and *(b)* geology (Jennings et al.,

1977) and topography (USGS) of the Cosumnes Watershed

161

### 3. Numerical Modeling Methods

In this section, we briefly describe the two numerical models that we used in this study:

(1) ParFlow-CLM, which simulates interactions as well as the transfer of water and energy

between the lower atmosphere, the land surface, and the subsurface, and (2) Weather Research

166 Forecast (WRF), which simulates mesoscale numerical weather prediction, and is used here to

167 drive the meteorological conditions of the ParFlow-CLM simulations.

## 3.1. Integrated Hydrologic Model: ParFlow-CLM

169 ParFlow-CLM (Kollet and Maxwell, 2006; Maxwell, 2013; Maxwell and Miller, 2005)

170 describes the movement of water in the subsurface by solving the three-dimensional mixed form

171 of Richards equation (Richards, 1931), given by:

$$172 \qquad S_S S_W(\psi_P)\frac{\partial \psi_P}{\partial t} + \phi \frac{\partial S_W(\psi_P)}{\partial t} = \nabla.\left[k(x)k_r(\psi_P)\nabla(\psi_P - z)\right] + q_s \qquad (1)$$

173 Where $S_S$ is the specific storage (L$^{-1}$), $S_W(\psi_P)$ is the degree of saturation (-) associated

174 with the subsurface pressure head $\psi_P$ (L), $t$ is the time, $\phi$ is the porosity (-), $k_r$ is the relative

175 permeability (-), z is the depth (L), $q_s$ is the source/sink term (T$^{-1}$), and $k(x)$ is the saturated

176 hydraulic conductivity (L T$^{-1}$). The interdependence of variables (i.e. relationships between

177 saturation and pressure head and between relative permeability and pressure head) is described

178 by the Van Genuchten model (van Genuchten, 1980). Overland flow is described by the two-

179 dimensional form of the kinematic wave equation given by:

$$180 \qquad -k(x)k_r(\psi_0)\nabla(\psi_0 - z) = \frac{\partial \|\psi_0, 0\|}{\partial t} - \nabla.\vec{v}\|\psi_0, 0\| - q_r(x) \qquad (2)$$

181 Where $\|\psi_0, 0\|$ indicates the greater term between $\psi_0$ the surface pressure-head and 0, $\vec{v}$

182 is the depth averaged velocity vector of surface runoff (L T$^{-1}$), $q_r$ represents rainfall and

183 evaporative fluxes (L T$^{-1}$). The depth of the ponding water at the surface in $x$ direction ($v_x$) and $y$

184 direction ($v_y$) is calculated by:

$$185 \qquad v_x = \frac{\sqrt{S_{f,x}}}{n}\psi_0{}^{2/3} \text{ and } \quad v_y = \frac{\sqrt{S_{f,y}}}{n}\psi_0{}^{2/3} \qquad (3)$$

186 Where $S_{f,x}$ and $S_{f,y}$ are the friction slopes in the $x$ and $y$ directions (respectively), and $n$ is

187 the manning coefficient.

188        Solutions of the Richards and kinematic wave equations require the terms $q_s$ and $q_r(x)$

189    respectively. These terms include the land surface processes simulated by CLM, such as

190    evapotranspiration, infiltration, and snow dynamics. To compute these processes, CLM uses soil

191    moisture calculated by ParFlow, vegetation characteristics (the type of land use/land cover as

192    well as its physical properties), and the meteorological forcing calculated by WRF.

193        The Cosumnes ParFlow-CLM model is horizontally resolved at 200 m and varies in

194    vertical discretization from 10 cm at the land surface to 30 m at the bottom of the domain. The

195    total thickness of the domain is 80 m. An analysis of variations in measured groundwater levels

196    showed that this thickness is sufficient to capture water table depth fluctuations and that in

197    general, beyond 50 m below the ground surface the aquifer remains fully saturated. Simulations

198    utilize parallel high-performance computing to accommodate the large number of cells

199    (approximately 1.4 million) that constitute the high-resolution model.

200        The Cosumnes watershed is bounded by the American and Mokelumne rivers and is

201    constrained in the model with the use of weekly-varying values of Dirichlet boundary conditions

202    along these borders. A no-flow (i.e. Neumann) boundary condition is imposed at the eastern,

203    headwater side of the watershed. Hydrodynamic properties (including hydraulic conductivity,

204    specific storage, porosity, Van Genuchten parameters) are derived from a regional geological

205    map (Geologic Map of California, 2015; Jennings et al., 1977) and a literature review of previous

206    studies (Faunt et al., 2010; Faunt and Geological Survey (U.S.), 2009; Flint et al., 2013; Gilbert

207    and Maxwell, 2017; Welch and Allen, 2014). The 2011 National Land Cover (NLCD) map

208    (Homer et al., 2015) is used in CLM to define land use and land cover. Agricultural maps

209    provided by the National Agricultural Statistics Service (NASS) of the US Department of

210    Agriculture's (USDA) Cropland Data Layer (CDL) (Boryan et al., 2011) are used to further

211  delineate specific croplands in the Central Valley. Vegetation parameters are defined by the

212  International Geosphere-Biosphere Programme (IGBP) database (IGBP, 2018). The developed

213  model also accounts for pumping and irrigation occurring in the Central Valley. More details

214  about the model parameterization and validation can be found in Maina et al., (2020) and Maina

215  and Siirila-Woodburn, (2020).

216       A full water year is simulated to demonstrate how different scales of meteorological

217  forcing impact both wet and dry seasons of the year.  The water year 2017 (i.e. October 1st, 2016-

218  September 30th, 2017), a particularly wet year, is selected to conservatively demonstrate how

219  forcing scales may impact hydrologic results in a wide range of weather conditions.

220

221       **3.2. Meteorological Model: Weather Research Forecast (WRF)**

222       WRF (Skamarock et al., 2008b; Skamarock and Klemp, 2008) is a state-of-the-art, fully

223  compressible, non-hydrostatic, mesoscale numerical weather prediction model. As shown in

224  Figure 2, we configure WRF version 3.6.1 over four two-way nested domains with a horizontal

225  resolution of 13.5 km (domain 1, d01), 4.5 km (domain 2, d02), 1.5 km (domain 3, d03), and 0.5

226  km (domain 4, d04). Each domain is composed of 30 vertical atmospheric levels. Land cover in

227  WRF matches the one used in ParFlow-CLM. Post-spin-up soil moisture from ParFlow-CLM is

228  used to initialize the WRF model at the beginning of the simulation. Other WRF initial

229  conditions, as well as boundary conditions, are defined based on the NLDAS-2 (Cosgrove et al.,

230  2003) terrestrial and meteorological data. The lateral boundary condition is specified for the

231  coarse grid (d01 in Figure 2) to constrain wind speed and direction, potential temperature,

232  mixing ratio for water vapor, geopotential height, and hydrostatic pressure. The parametrizations

233  that represent physical processes in the configuration of WRF used here include the Dudhia

234  scheme (Dudhia, 1988) for shortwave radiation, the Rapid Radiative Transfer Model (Mlawer et

235  al., 1997) for longwave radiation, the Morrison double-moment scheme (Morrison et al., 2009)

236  for microphysics, University of Washington Boundary Layer Scheme (Bretherton and Park,

237  2009) for the planetary boundary layer, and the Eta Similarity scheme (Monin and Obukhov,

238  1954) for the model surface layer. The Grell-Freitas scheme (Grell and Freitas, 2014) is used for

239  cumulus parameterization in two outer-most domains only (d01 and d02). For domain d03 and

240  d04, the higher-resolutions allow for convection to be resolved explicitly. WRF mass balance

241  validation results are shown in Appendix A1. The described configuration of WRF has been

242  extensively validated against ground observation of meteorological conditions in the California

243  region in previous works (Vahmani et al., 2019; Vahmani and Jones, 2017). These studies show

244  a very good performance for the current configuration of WRF over California, predicting daily

245  mean and maximum air temperatures and evapotranspiration with errors of 1.1 °C, 0.4 °C, and

246  0.74 mm day$^{-1}$, respectively. We further compare WRF simulations over the Cosumnes

247  watershed with ground measurements (see Appendix A3). Our comparisons indicate a reasonable

248  match between measurements and simulations allowing us to gain confidence in the ability of

249  WRF to reproduce the atmospheric dynamics in this watershed.

250      Using the nested domain configuration of WRF described above, we design a series of

251  simulations to dynamically downscale across the four spatial resolutions. The coarsest scale of

252  forcing at 40.5 km resolution is generated by statistically up-scaling the coarsest of the WRF

253  simulations (13.5 km). WRF simulations are conducted from September 1$^{st}$, 2016 to September

254  30$^{th}$, 2017, covering the entire water year 2017 plus one month of spin-up. Spatial distributions

255  of precipitation and temperature at three selected times (characterized by three different storms

256    of varying intensity and duration) obtained with the five spatial resolutions of forcing are shown

257    in Appendix A2.
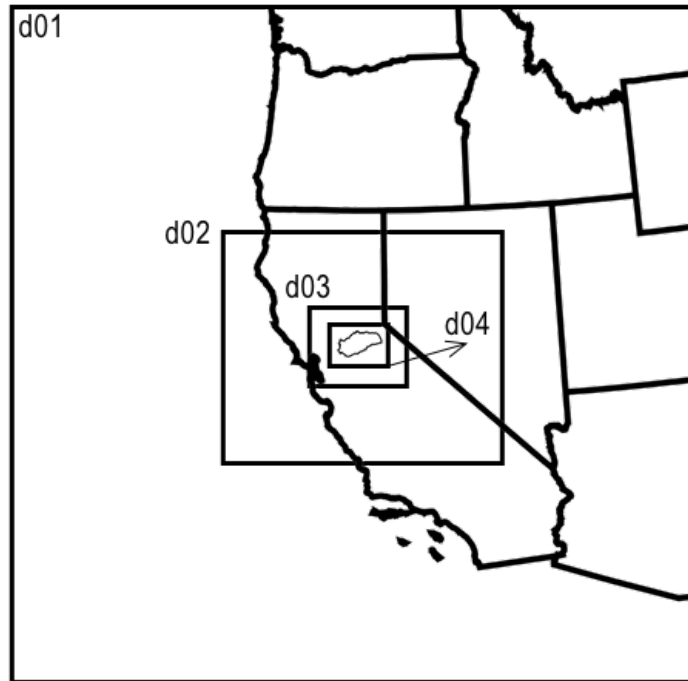
258

259    Figure 2: Geographical representation of four WRF nested domains with 13.5, 4.5, 1.5, and 0.5

260    km spatial resolutions for d01, d02, d03, and d04, respectively.

261

262        **3.3. Hydrologic variables**

263        Results from the five spatial resolutions are compared for key land surface and

264    subsurface processes. We consider the results obtained with the finest spatial resolution of

265    meteorological forcing (0.5 km, closest to that of the hydrologic model) as the most accurate

266    resolution, and evaluate the differences relative to that of the four remaining resolutions (1.5, 4.5,

267    13.5 and 40.5 km). Comparisons are shown as an absolute error (*AE*) and/or percent error (*PE*)

268    relative to the 0.5 km results via:

269        $$AE_{i,t} = X_{0.5_{i,t}} - X_{R_{i,t}} \tag{5}$$

270        and

271    $$PE_{i,t} = \frac{X_{0.5_{i,t}} - X_{R_{i,t}}}{X_{0.5_{i,t}}} \times 100 \qquad\qquad (6)$$

272    where $X$ is the model output (*ET, I, SWE,* or $\psi$) at a given point in space (*i*) at a time (*t*), and *R* is

273    the spatial resolution of the forcing (1.5, 4.5, 13.5 or 40.5 km). Snap-shots in time of these errors

274    highlight the sensitivity of each scale of forcing in space. Global (i.e. domain-wide) differences

275    are also calculated for select parameters of interest and shown as a function of time.

276    Because large-scale changes in storage are of interest from a water management

277    perspective, total surface water (SW) storage is calculated via:

278    $$Storage_{SW} = \sum_{i=1}^{n_{SW}} \Delta x_i \times \Delta y_i \times \psi_i \qquad\qquad (7)$$

279    where $n_{SW}$ is the total number of river cells (-), $\Delta x_i$ and $\Delta y_i$ are cell discretizations along

280    the x and y directions (L), and *i* indicates the cell. Similarly, total groundwater (GW) storage is

281    calculated via:

282    $$Storage_{GW} = \sum_{i=1}^{n_{GW}} \Delta x_i \times \Delta y_i \times \Delta z_i \times \psi_i \times (S_{s_i}/\phi_i) \qquad\qquad (8)$$

283    where $n_{GW}$ is the total number of subsurface saturated cells (-) and $\Delta z_i$ is the

284    discretization along the vertical direction the cell (L).

285

286    **4.  Results and discussions**

287      **4.1.Snow Water Equivalent, *SWE***

288    Figure 3 shows the domain total *SWE* obtained with the five resolutions of forcing. Our

289    results indicate that all four resolutions overestimate the *SWE* when compared to the results

290    obtained with 0.5 km forcing. We note that the accumulation of *SWE* starts at the same time for

291    all resolutions while the time of snowmelt peak varies considerably from one resolution to

292    another, the coarser resolutions show a delay in ablation. For example, *SWE* results obtained

293    with the 40.5 km resolution forcing exhibits low global error for the first half of the water year,

294  however during peak ablation the differences are very large both in terms of magnitude ($PE = 90$

295  %) and timing (which is delayed by around 40 days). Our results show that an accurate

296  representation of *SWE* requires forcing data with a resolution close to that of the hydrologic

297  model. This conclusion is somewhat different from that drawn by Rasmussen et al., (2011), who

298  found that the representation of *SWE* in mountainous systems can be accurate for spatial

299  resolutions of forcing lower than 6 km. A possible explanation for this difference is the

300  resolution of the physics-based model used in this study compared to that of Rasmussen and co-

301  authors, the integrated hydrologic model we used in addition to the climate model, or differences

302  stemming from watershed locations of the two studies.
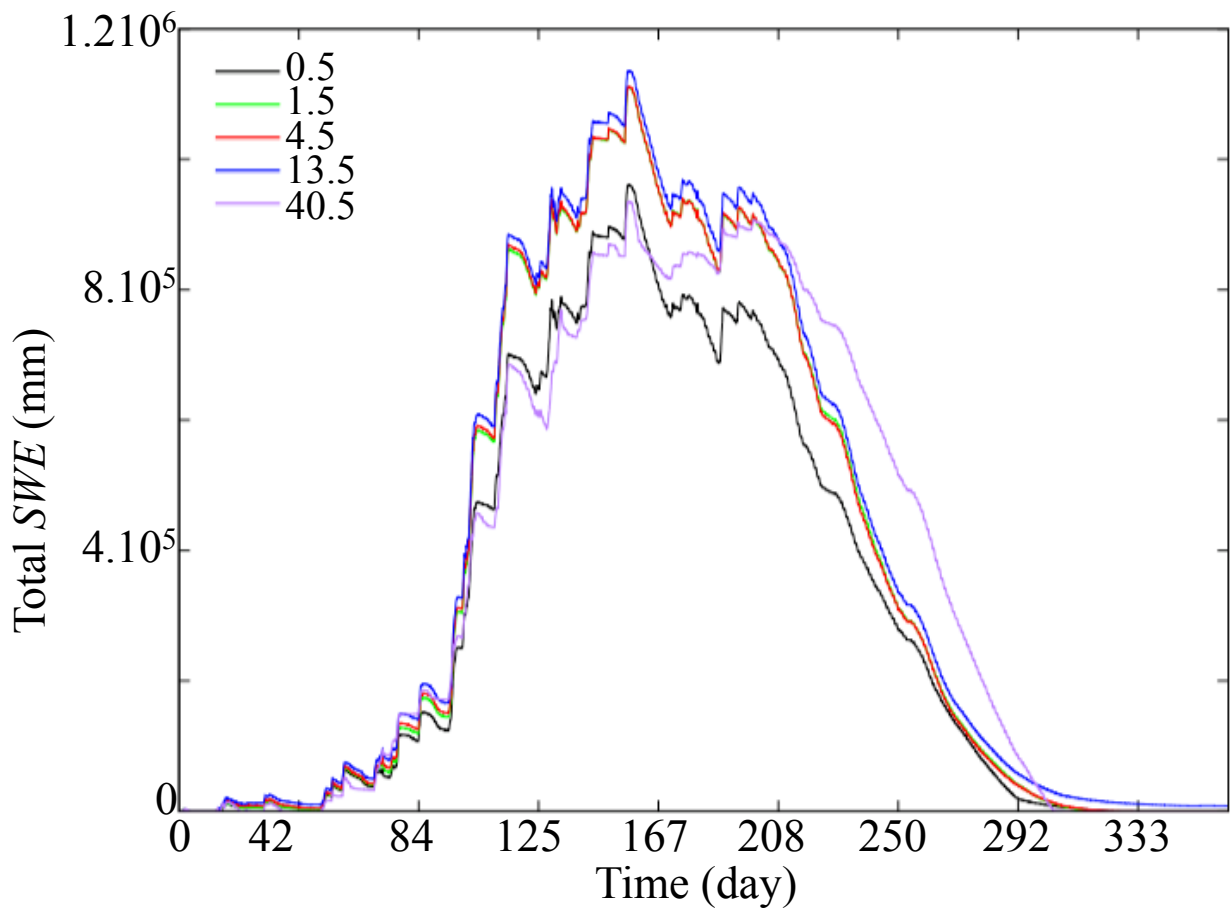
303

304 Figure 3: Temporal variations of the total Snow Water Equivalent *(SWE)* obtained with

305 meteorological forcing at spatial resolutions of 0.5, 1.5, 4.5, 13.5, and 40.5 km.

306

307 Figure 4a shows the spatial distributions of *SWE* obtained with the five spatial resolutions

308 at two selected days, which correspond to the beginning (January) and peak (March) of snow

309 accumulation. The spatial distribution of *SWE* is more precise for results obtained with the

310 higher resolution meteorological forcing. *SWE* distributions obtained with meteorological forcing

311 of resolutions at or above 13.5 km are not well estimated. Figure 4b shows the spatial

312 distribution of the absolute error of *SWE* ($AE_{SWE}$). Over- and under- estimations of *SWE* with

313 similar magnitudes are observed for all the four resolutions. Errors in *SWE* distribution increase

314 (with *AE* greater than 100 mm) as the resolution of the forcing data decreases. We notice that

315 over- and under- estimations of *SWE* depend both on the topography and the resolution of

316 forcing as snow processes depend not only on the meteorological conditions but also on the slope

317 and aspect of a given hillslope. Depending on the elevation, the orientation of the cell (north and

318 south facing), the energy fluxes are different resulting in very different snow dynamics. This

319 strengthens the conclusions drawn previously stating that the meteorological data should be at a

320 resolution close to the one associated with the input data (e.g. topography) as well as the physics-

321 based model to ensure a good precision and accuracy in the representativity of the snow

322 dynamics. We further note that differences in *SWE* will lead to different snowmelt, *ET,* and

323 infiltration rates which will have implications for other hydrologic variables such as streamflow

324 and groundwtaer levels.

325
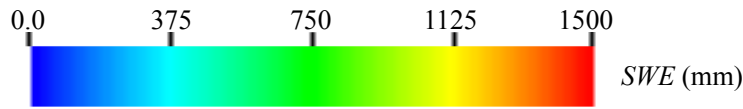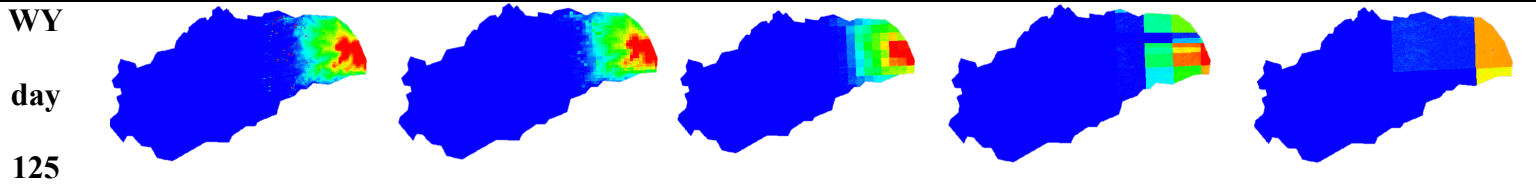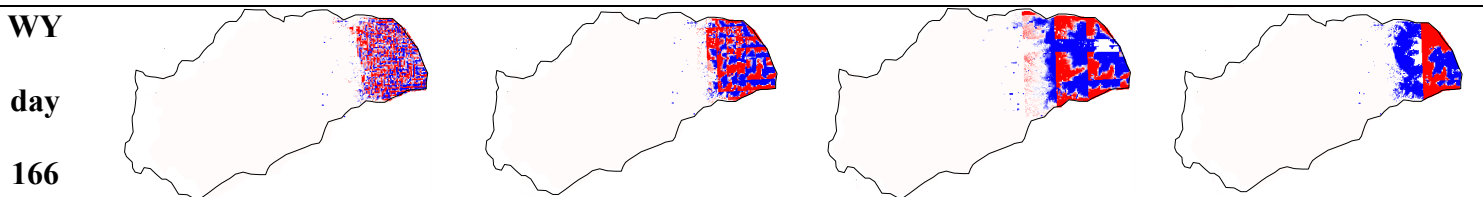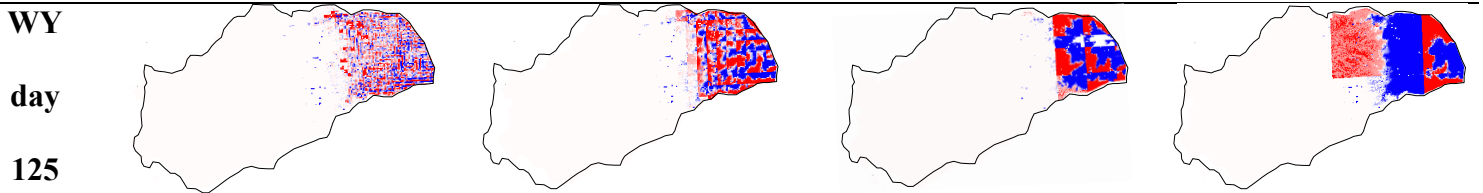
Figure 4: Spatial distributions of *(a)* the *SWE* obtained with the five spatial resolutions of meteorological forcing and *(b)* absolute error of *SWE* ($AE_{SWE}$) with respect to the highest spatial

331     resolution of meteorological forcing (0.5 km). Results are shown at WY days 125 (January) and

332     166 (March).

333

## 4.2. Evapotranspiration, *ET*

335       Figure 5 shows the temporal variation of the percent error in the domain-average *ET*

336    ($PE_{ET}$) flux as calculated with equation (6). We note that the percent error has large values due to

337    the low values of *ET*; thus small changes in *ET* result in large percent errors. While in general,

338    the coarsest spatial resolution of forcing (i.e. 40.5 km) shows the highest errors for some time

339    steps, the percent errors obtained with the second coarsest meteorological forcing (13.5 km) are

340    actually the largest. A possible explanation is the aggregated nature of the domain-average *ET*.

341    Depending on the time step, the coarser forcing resolutions can lead to either an over or under-

342    estimation of *ET*. Results do not show a systematic trend with regards to the over- or under-

343    estimation of *ET*. It is therefore difficult to establish a clear relationship between the spatial

344    resolution of forcing and the directionality of *ET* error at a watershed scale. Note, however, that

345    these errors do not increase over time. This can be related to the fast-changing nature of *ET* that

346    is strongly linked to short-lived weather patterns and the diurnal cycle.

347
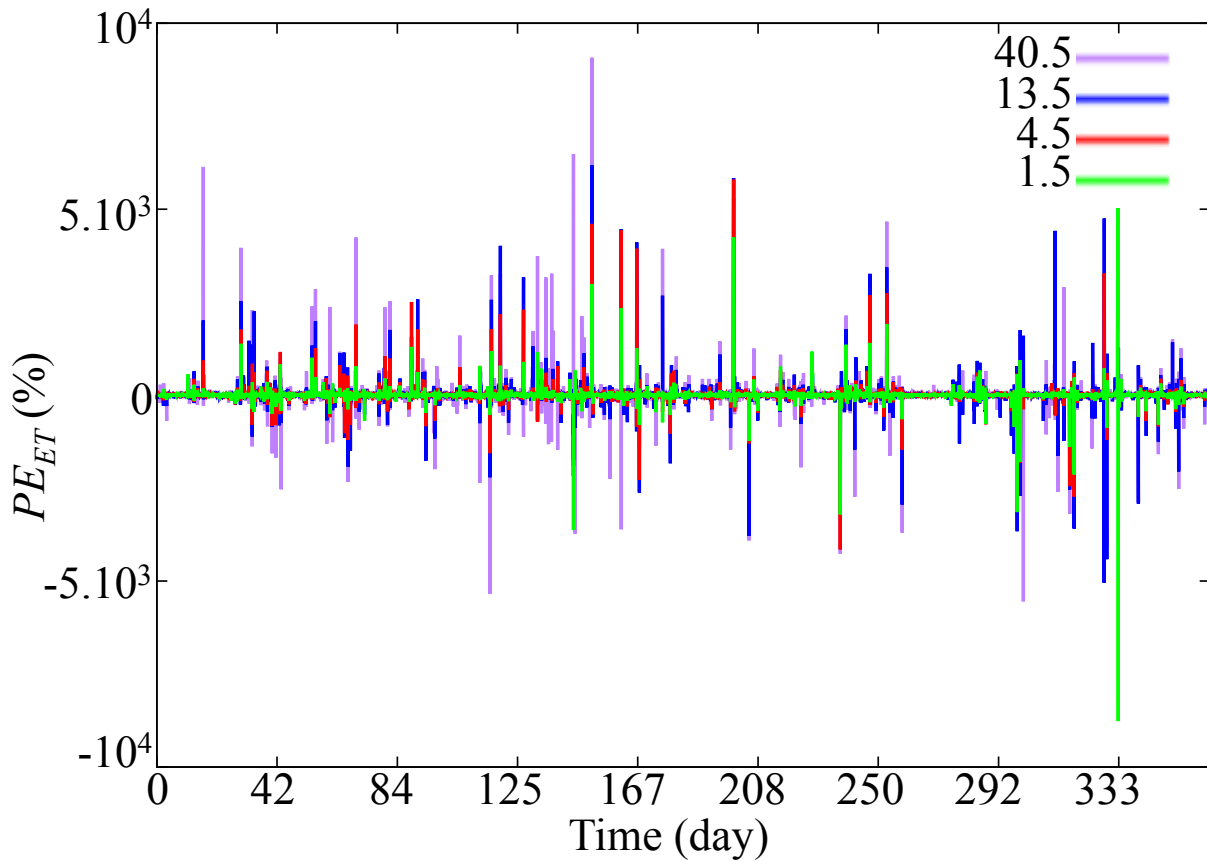
Figure 5: Temporal variation of the percent error of evapotranspiration, $PE_{ET}$, obtained with

meteorological forcing at spatial resolutions of 1.5, 4.5, 13.5, and 40.5 km relative to the highest

spatial resolution of meteorological forcing (0.5 km)

351

Figure 6a shows the spatial distributions of $ET$ for the five resolutions at two selected

time steps characterizing periods with and without precipitation events. Day 0 corresponds to a

dry day in October and day 167 corresponds to a wet day in March. The spatial patterns of $ET$ at

these two time steps are different. Furthermore, spatial patterns between the different scales of

forcing also reveal distinct $ET$ patterns. As expected, the most accurate $ET$ distribution is

obtained with the highest resolution of the meteorological data, the coarser a resolution of

meteorological data is the less accurate the spatial distribution of $ET$. Because the highest

359 resolution of forcing is close to the resolution of the integrated hydrologic model (and thus the

360 resolution of input data such as topography, geology, and land use and land cover), it allows us

361 to better understand the relationships between *ET* and these different characteristics of the

362 watershed. Such analyses are difficult to undertake for coarser resolutions.

363

364

365
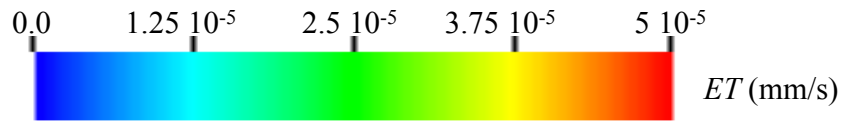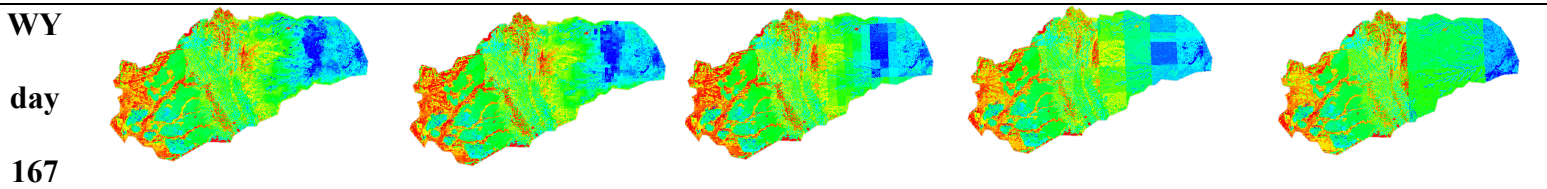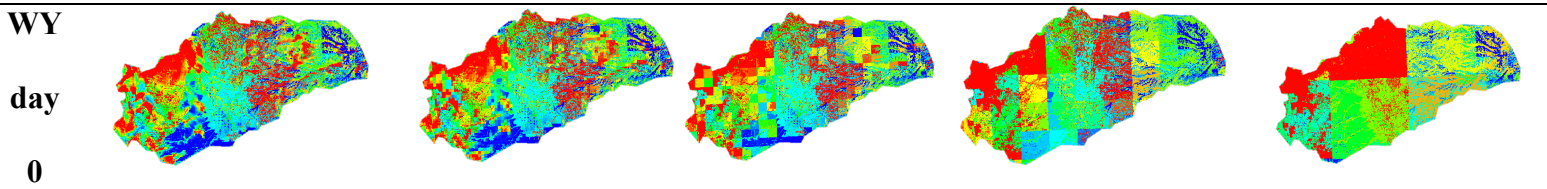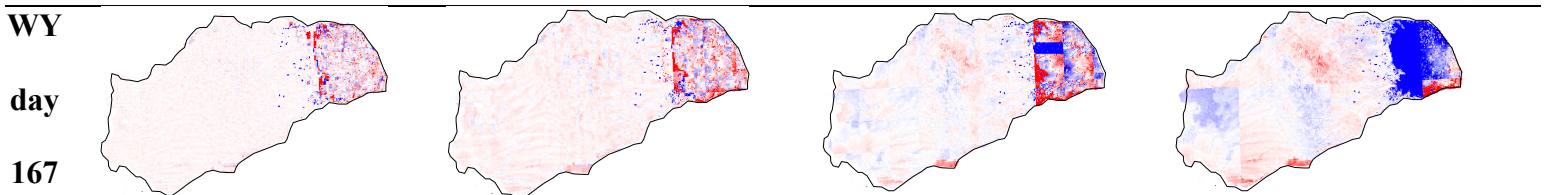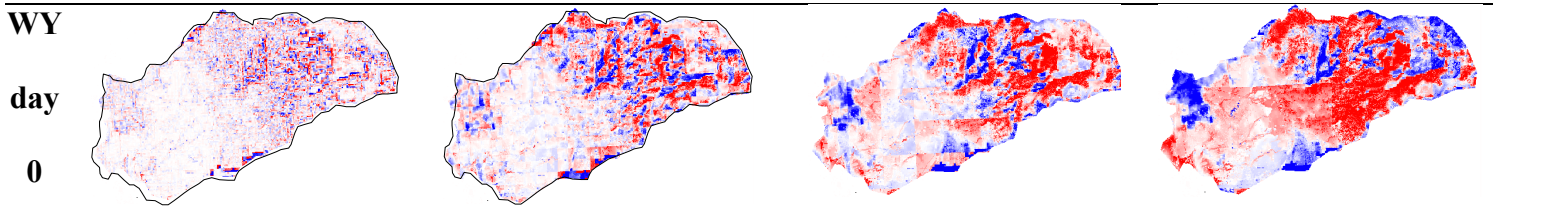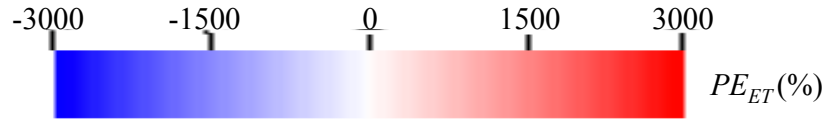
$PE_{ET}$(%)

366

367    Figure 6: Spatial distributions of *(a)* the *ET* obtained with the five spatial resolutions of

368    meteorological forcing and *(b)* percent error of *ET* (*PE$_{ET}$*) with respect to the highest spatial

369    resolution of meteorological forcing (0.5 km). Results are shown at the first day of the simulation

370    (WY day 0, in October) and during the time at which peak differences are observed (WY day

371    167, in March).

372

373         Seasonality and location affect the degree to which forcing scales impact *ET*. Note that

374    for the spatial distributions of *ET* associated with the second time step considered (day 167), the

375    results obtained with the five resolutions are very similar in the Central Valley. At this time

376    spatial patterns of *ET* only differ in the Sierra Nevada Mountains and the intrusion. The geology,

377    as well as, the land cover and the topography are more or less uniform in this valley, whereas

378    these parameters notably topography vary significantly in the Sierra Nevada Mountains. For the

379    first time step, the differences observed in the Central Valley are due to the fact that for very

380    precise resolutions of the forcing, the evolution of the storm is accurate (see Appendix A2) and

381    so is the *ET*. Thus, for relatively homogeneous areas such as the Central Valley, high-resolution

382    forcing data is required only if the storm shows a strong spatial variation within the areas

383    whereas for highly heterogeneities associated with geology, topography, and land-cover, high-

384    resolution forcing data are always required if one is interested in analyzing accurately the spatial

385    distribution of *ET*.

386         Figure 6b shows the spatial distributions of percent error of *ET* (*PE$_{ET}$*) relative to the

387    results of the 0.5 km meteorological forcing. Whatever the resolution considered, we note both

388    an over- and under- estimation of *ET* on the same scale of error (+/- 3000%), but with more

389    localized and less wide-scale differences at the finest scale of meteorological forcing. We also

390    observe that error is higher in the Sierra Nevada Mountains characterized by complex

391    topography and geology than in the Central Valley for all resolutions. This reinforces the

392    conclusions drawn previously, namely that for complex environments a precision in the

393    meteorological data is strongly required.

394

395    **4.3.Infiltration**

396    Figure 7 shows the spatial distributions of infiltration obtained with the five spatial

397    resolutions (Figure 7 a) and their corresponding percent errors (Figure 7 b) at two selected times

398    corresponding to winter (WY day 83, December, presence of precipitation event) and summer

399    (WY day 291, June, absence of precipitation event). The first time step corresponds to the snow

400    accumulation period while the second one characterizes the snowmelt period. The spatial

401    resolution of forcing data strongly impacts the spatial distribution of infiltration. Indeed, for

402    coarse resolutions (i.e. 40.5 km), it is almost impossible to determine the position of the storm

403    and its impact on infiltration, the results obtained at this scale are strongly dependent on the

404    resolution of the forcing. However, for more precise resolution (i.e. 0.5 km), we can exactly see

405    the location of the storm, this resolution allows distinguishing areas characterized by a very weak

406    infiltration as the upper part of the catchment corresponding to the Sierra Nevada Mountains.

407    Indeed, in this area, due to the accumulation of snow (precipitation is in the form of snow unlike

408    in the Central Valley), the resulting infiltration is zero. The spatial extension of the area subject

409    to the snow accumulation is only accurate for high-resolution meteorological forcing results.

410                                                       *(a)*
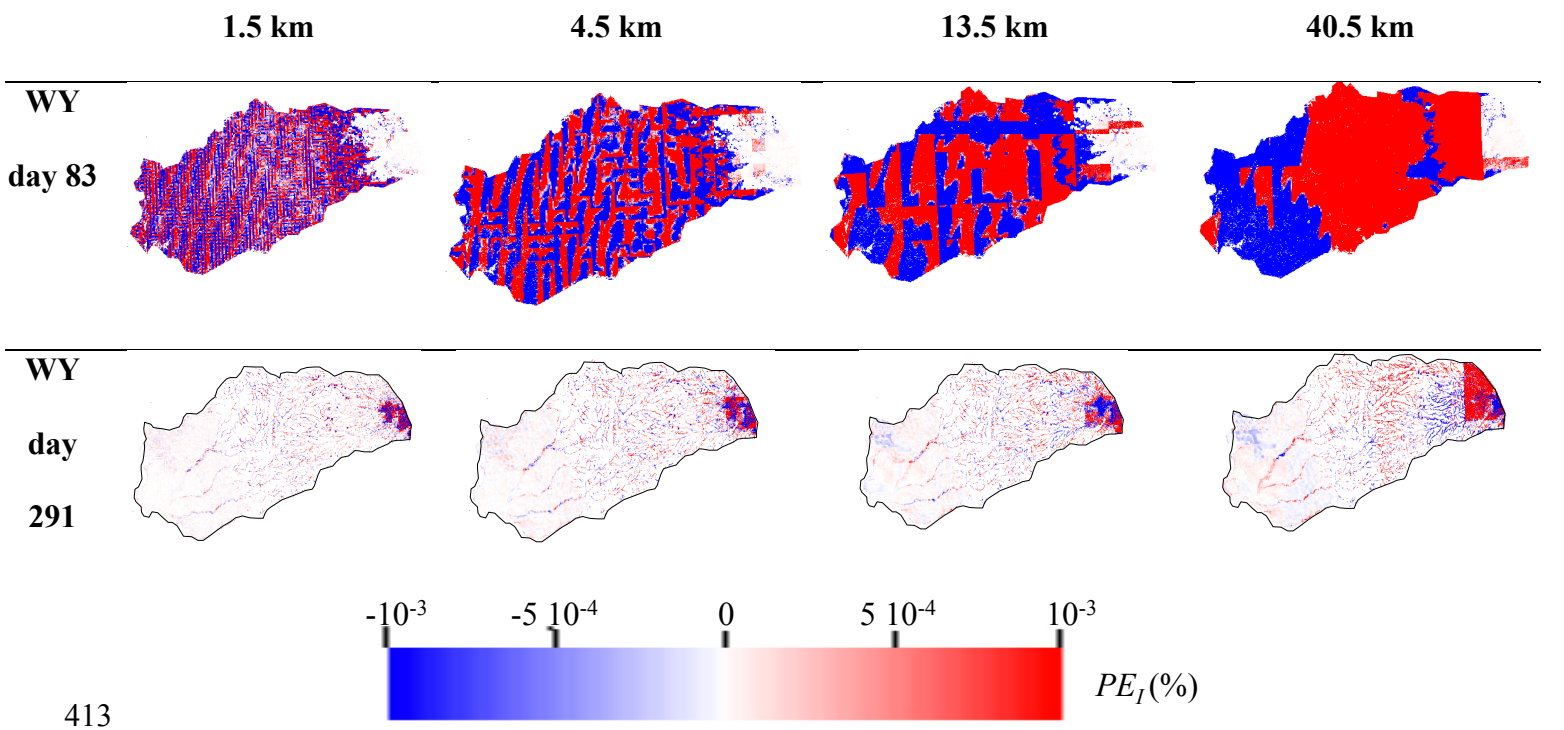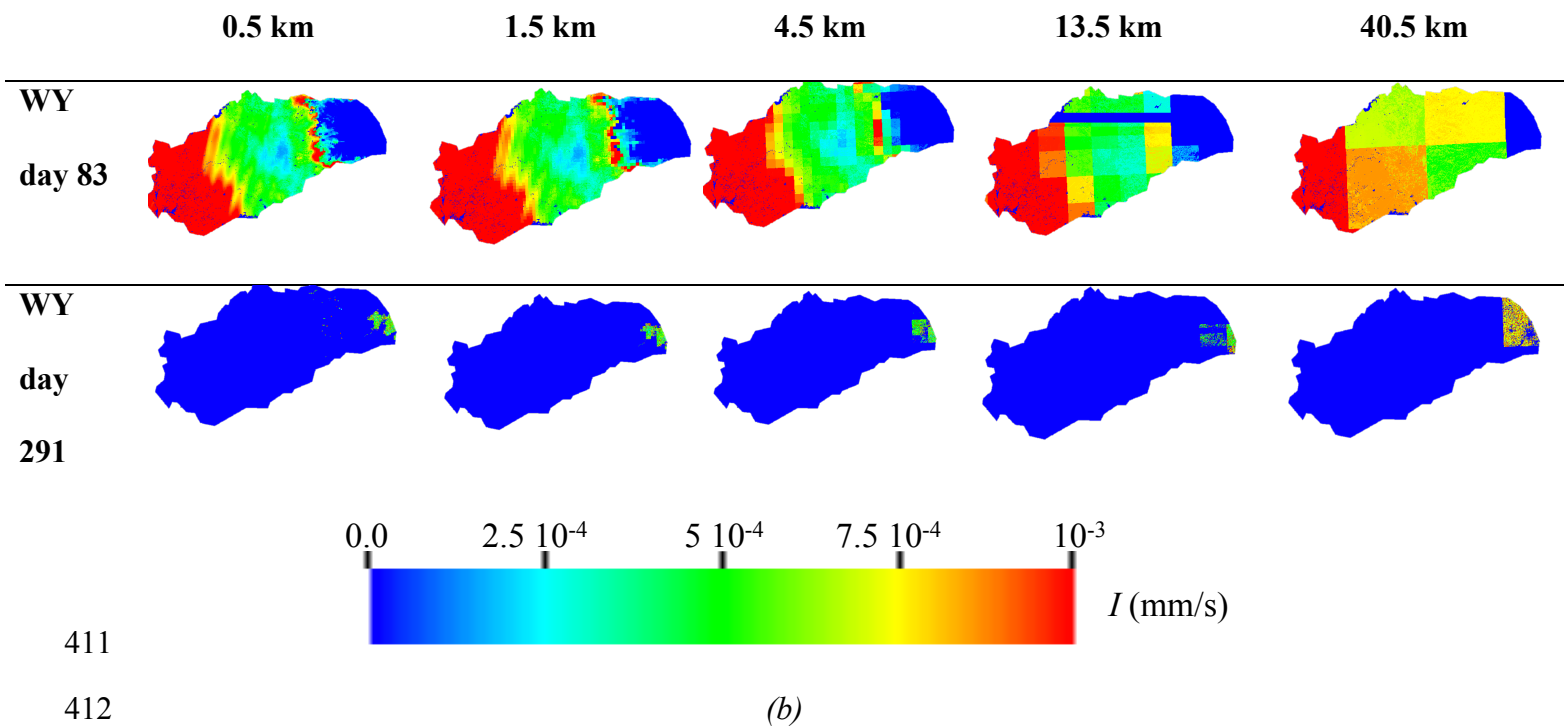
Figure 7: Spatial distributions of *(a)* infiltration *I* obtained with the five spatial resolutions of

meteorological and the *(b)* percent error of infiltration (*PE_I*) with respect to the highest spatial

416    resolution of meteorological forcing (0.5 km). Results are shown in winter (WY day 83) and

417    summer (WY  day 291).

418

419         To better understand how the quality and precision of the spatial distribution of

420    infiltration deteriorates by decreasing the resolution of the input data, Figure 7b shows the spatial

421    distribution of the $PE_I$ of the four resolutions at the same two time steps. For the first time step,

422    the errors are null in the Sierra Mountains which is not the case for the second time step.

423    Whatever the resolution considered, and as previously discussed, we note that depending on the

424    point considered there may be over- and under- estimation of the infiltration with percent error

425    close to $10^{-3}$. Note that these differences are observed over the entire watershed except in the

426    Sierra Mountains for the first time step, while for the second time step, these errors are only

427    observed along the river and its tributaries as well as in the Sierra Nevada Mountains. This

428    second time step corresponds to the summer, a snowmelt period and without rain. As such,

429    differences of infiltration in the Sierra Nevada Mountains are due to the snowmelt. As for the

430    differences observed close to the areas subject to the overland flow, these are due to the

431    exchanges between the surface flow and the subsurface. Because the amount of snow

432    accumulated as well as the spatial extent of the area subject to snow dynamics is different for the

433    five resolutions considered, the resulting snowmelt is different. Thus, the runoff controlled by

434    this snowmelt will also be different and so is the infiltration of the quantities of water coming

435    from the overland flow. This indicates that the effects of the spatial resolution of forcing data can

436    be delayed in time.

437

438         **4.4. Surface and subsurface flow**

### 4.4.1. Surface water storage and river stage

Figure 8 illustrates the percent error of surface water storage $PE_{SW}$. In general, the percent error of the surface water storage is small (< 5%) regardless of the time of the year, and these differences are almost zero for the results obtained with 1.5 and 4.5 km forcing resolutions for the entire water year. As shown in Figure 9 illustrating the spatial distributions of the absolute error of surface pressure-head ($AE_{\Psi_S}$), the percent error of the total surface water storage at the watershed scale is small because some regions in the domain over-estimate the pressure-head while others under-estimate the pressure-head. In contrast, while the error is negligible at the beginning of the simulation for results obtained with forcing at 13.5 and 40.5 km, the $PE_{SW}$ increases over time, eventually reaching a near-maximum at the end of the water year. This suggests that $PE_{SW}$ may be cumulative and that longer simulations with overly coarse scales of forcing will compound through time. It's interesting to also note that while the results obtained with the 13.5 km resolution forcing overestimates the surface water storage at any time, those obtained with the 40.5 km resolution forcing show over-estimates of $PE_{SW}$ at the beginning of the simulation and under-estimates of $PE_{SW}$ at the end of the simulation. Moreover, the errors obtained with the 13.5 and 40.5 km resolution are of the same order but opposite signs. This suggests that although the total water budget is nearly equivalent for each scale of forcing considered here (see Appendix A1), an inaccurate spatial distribution of forcing can lead to an inaccurate redistribution (and possibly a delay) of water and energy, and hence different signals of surface water storage.

459
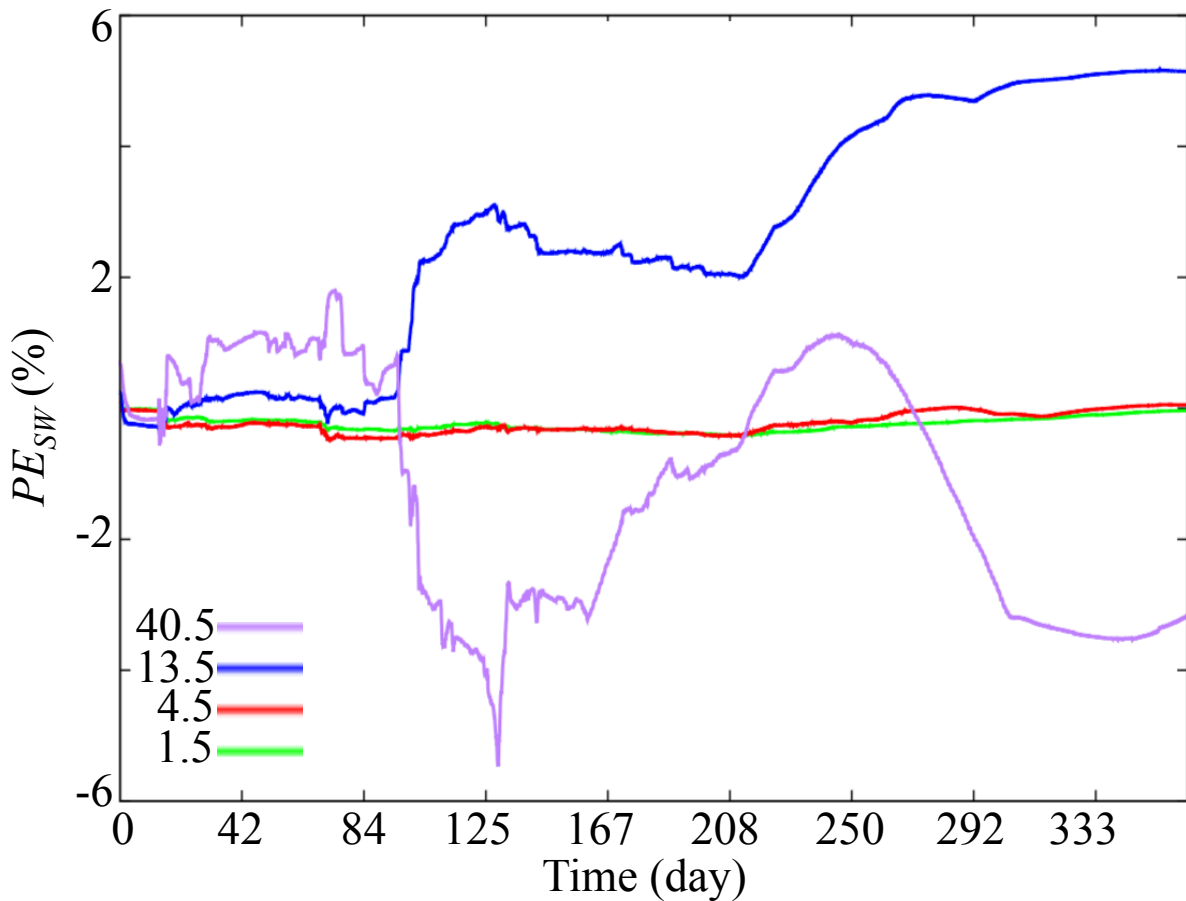
Figure 8: Temporal variations of the percent error of surface water storage ($PE_{SW}$) obtained with

meteorological forcing at spatial resolutions of 1.5, 4.5, 13.5, and 40.5 km with respect to the

highest spatial resolution of meteorological forcing (0.5 km)

463

Figure 9 shows the spatial distributions of the absolute error of pressure-head for the first

layer ($AE_{\Psi_S}$) at two selected time steps corresponding to winter (WY day 83, in December) and

summer (WY day 333, in August). Similar to $PE_{SW}$, this error increases with time. In December,

the error is nearly zero for forcing spatial resolutions of 1.5 and 4.5 km whereas it is non-zero

(with values close to 1 m) in August. Although the spatial resolutions of 13.5 and 40.5 km have

non-zero errors at the first time step, the error increases considerably as the simulation proceeds.

470  We note that the areas sensitive to the spatial resolution of the meteorological forcing data are

471  approximately the same for all four resolutions. Indeed, the absolute error is null at the intrusion

472  on contrary to the Central Valley and in the Sierra Nevada Mountains. Interestingly, these two

473  zones have different areas of influence, in the Central Valley, the errors are non-zero everywhere

474  except close to the river, which is contrary to the trend observed in the Sierras. This is related to

475  the geological nature of these environments. Due to the very low permeability and low surface

476  roughness of Sierra Nevada Mountains, any water from precipitation will quickly contribute to

477  surface runoff, which is highly sensitive to the spatial resolution of forcing, on contrary to the

478  Central Valley characterized by high permeability and low manning coefficient and therefore

479  low overland flow.
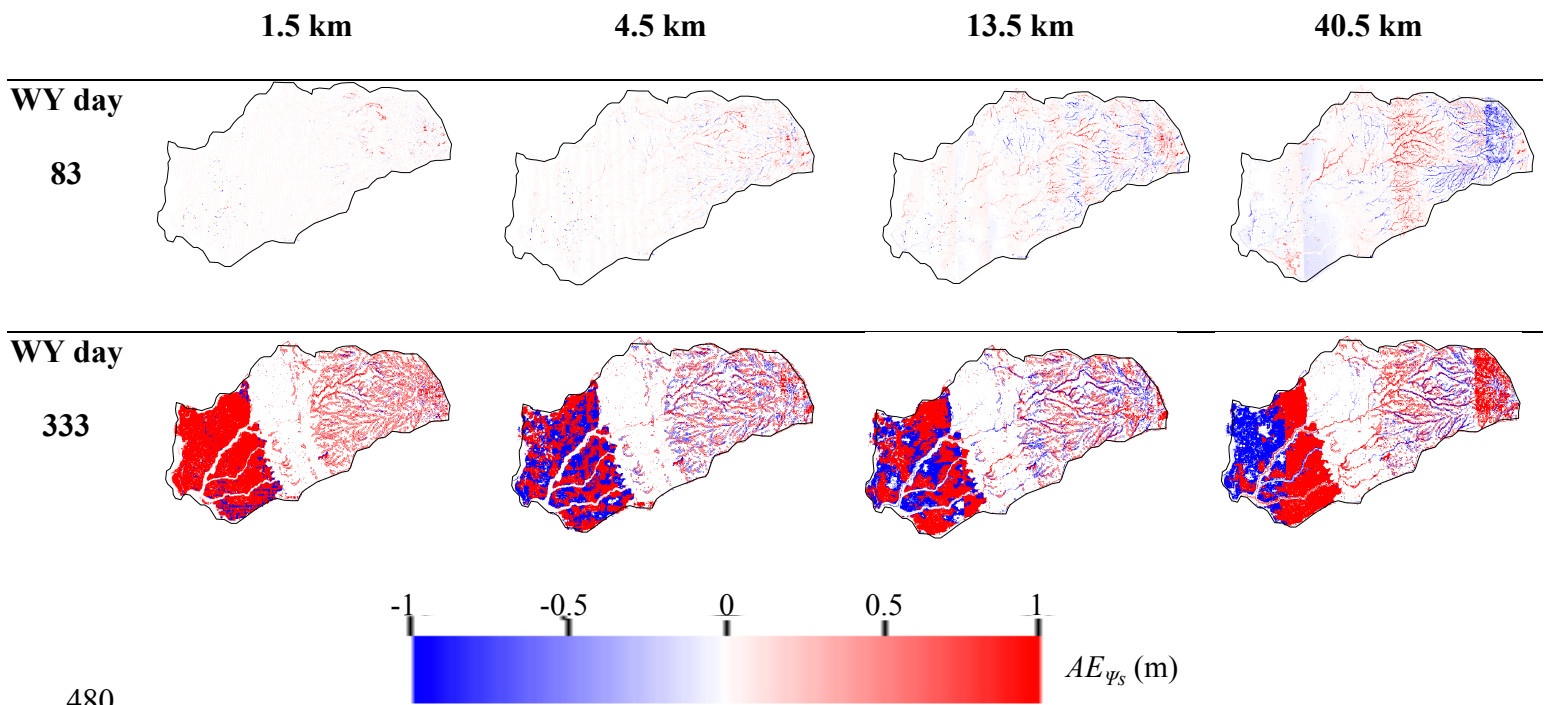
480

481  Figure 9: Absolute error of surface pressure-head ($AE_{\Psi_S}$) with respect to the highest spatial

482  resolution of meteorological forcing (0.5 km). Results are shown in winter (WY  day 83, in

483  December) and summer (WY  day 333, in August).

484

485      Within the water year, the maximum absolute error of surface water levels, max($AE_{\Psi_s}$), is

486  an important metric for understanding where, and to what degree, forcing resolution impacts the

487  prediction of river dynamics. Figure 10 shows the spatial distribution of max($AE_{\Psi_s}$), which is

488  obtained by an analysis of the maximum difference in surface water levels between the results

489  obtained with the highest spatial resolution of forcing (0.5 km) and the four other resolutions for

490  all time steps. Maximum differences in surface water levels are shown in absolute values (in

491  units of meters) and are at any point in time in the simulated water year. Differences in surface

492  water levels at a given time are as high as 3 m. High values of differences are mainly located in

493  the headwater region of the watershed, although some lower regions of the model such as one

494  tributary of the main stem of the Cosumnes near the river outlet also show max($AE_{\Psi_s}$) as high as

495  3 m. These results suggest that although the impact of forcing spatial resolutions on the global

496  (i.e watershed-scale) surface water storage is small to insignificant (see Figure 8), at a given

497  point in space and time, differences may be considerable. This can be especially problematic for

498  calibration and validation purposes where input parameters of the model are adjusted to

499  reproduce the observed surface water levels with the model. In this case, differences between

500  measured and simulated hydrologic variables are assumed to be due to parametric uncertainties,

501  when in reality the source of the error is the scale of the meteorological forcing. Adjusting the

502  model parameters may potentially cause the model to inaccurately simulate the physics of the

503  system.

504

505

Figure 10: Spatial distributions of the maximum of Absolute Error of river height max($AE_{\Psi_S}$) with respect to the highest spatial resolution of meteorological forcing (0.5 km).

508
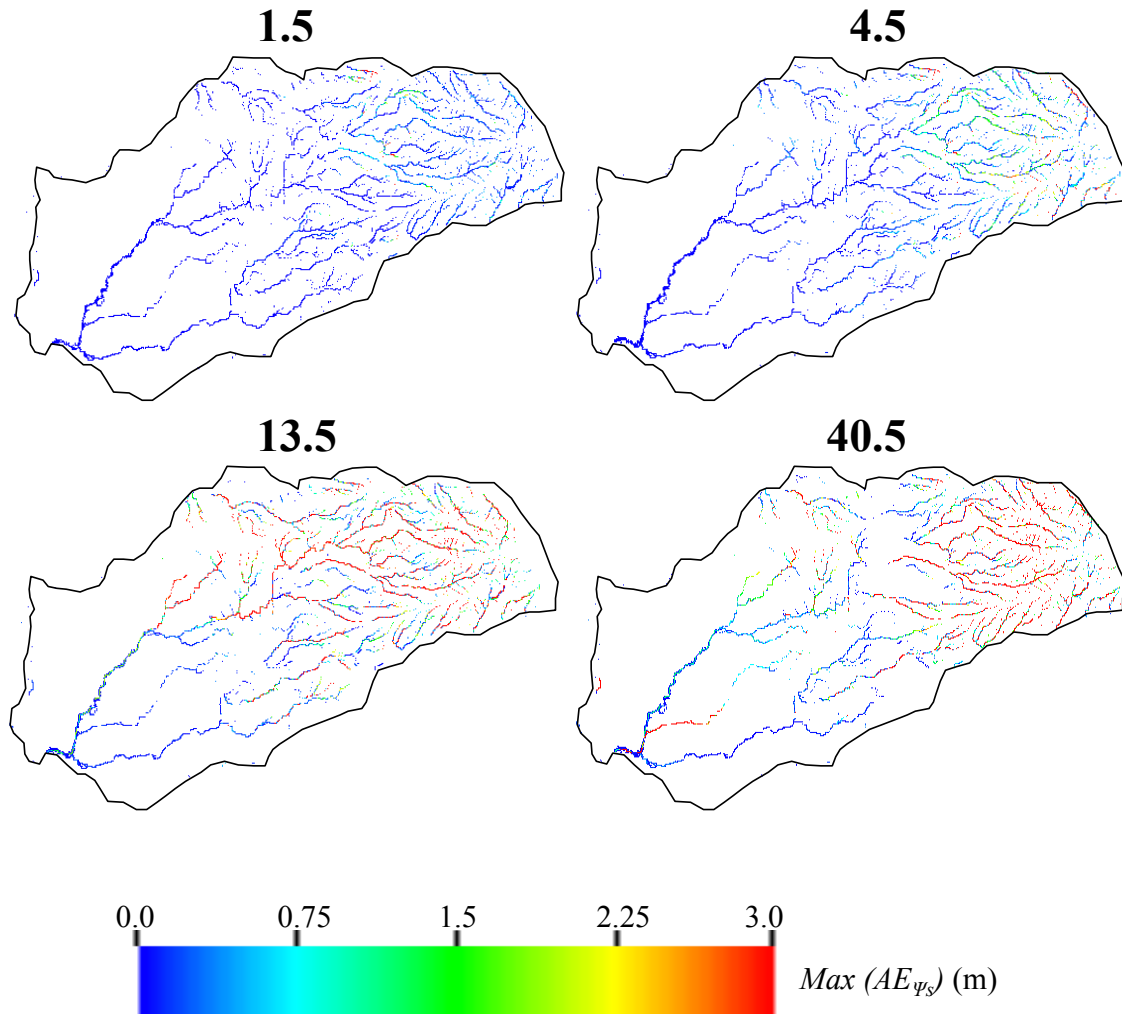
### 4.4.2. Groundwater storage and water table depth

Figure 11 depicts the percent error of groundwater storage $PE_{GW}$. For the cases considered here, the different spatial resolutions of forcing have very little impact on the total groundwater storage of the watershed.
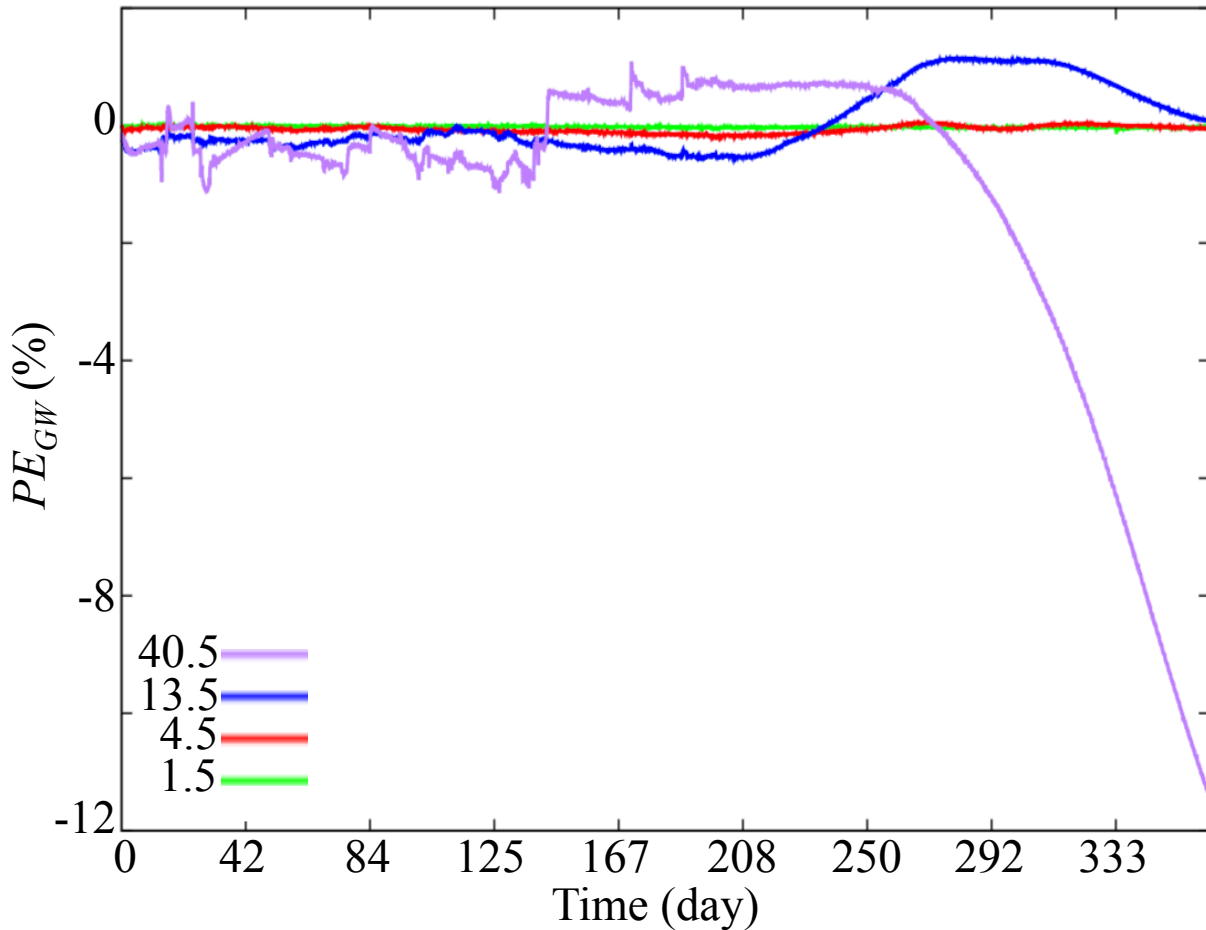
515    Figure 11: Temporal variations of the percent error of groundwater storage ($PE_{GW}$)

516    obtained with meteorological forcing at spatial resolutions of 1.5, 4.5, 13.5, and 40.5 km with

517    respect to the highest spatial resolution of meteorological forcing (0.5 km)

518

519        With the exception of the coarsest scale of forcing resolution towards the end of the

520    simulation, the error in groundwater  storage for the different spatial resolutions of forcing yield

521    very similar results. Groundwater storage obtained with a forcing resolution of 13.5 km

522    overestimates the storage, however, this overestimation remains very low, on the order of 1% at

523    most times. In contrast, the groundwater storage results obtained with the 40.5 km forcing

524    resolution are close to the storage obtained with the finest scale of forcing resolution at the

525    beginning of the simulation, yet these errors reach 10% at the end of the simulation.

526    Figure 12a shows the maps of Water Table Depth (WTD) absolute error ($AE_{WTD}$) for the

527    four scales of forcing resolution relative to the results obtained with the 0.5 km forcing. Water

528    year day 333 (August) corresponding to baseflow conditions is used here because differences in

529    water table depth at the beginning of the simulation are too small for interpretation. Results show

530    both an over- and under- estimation of the water table depth as a function of the forcing

531    resolution (Figure 12a). Thus, while the global groundwater storage error is low as indicated in

532    Figure 11, an examination of the spatial trends shows that this is predominantly due to the

533    counterbalancing of positive and negative error in space. For all the spatial resolutions

534    considered, the Sierra Nevada Mountains are the most sensitive areas to the spatial resolution of

535    meteorological data, while the intrusion remains insensitive with almost zero errors. This is due

536    to the characteristics of the Sierra Nevada Mountains which include strong variations of

537    topography, snow dynamics, and low permeability rocks. The intrusive zone is composed of

538    extremely low permeability materials so it has no groundwater dynamics, as such the errors are

539    zero. The spatial resolutions of 1.5 and 4.5 km have generally little impact on the water table

540    depth in the Central Valley alluvial aquifers. Larger errors in water table depths are mostly

541    observed for the results obtained with the 13.5 and 40.5 km forcing. These errors are not uniform

542    and are most significant along the Cosumnes River, its tributaries, and outside urban areas. The

543    connection between the upper and lower point of the watershed, as well as the integrated nature

544    of the system, is apparent in the maps of $AE_{WTD}$. As already discussed, because the spatial

545    resolution of forcing impacts snowpack dynamics, evapotranspiration and infiltration rates and

546    patterns, streamflow distributions, it, therefore, impacts groundwater dynamics and the exchange

547     of groundwater and surface water. We highlight here that these differences accumulate over time

548     as indicated by the errors that increase as the simulation progresses.

549

552
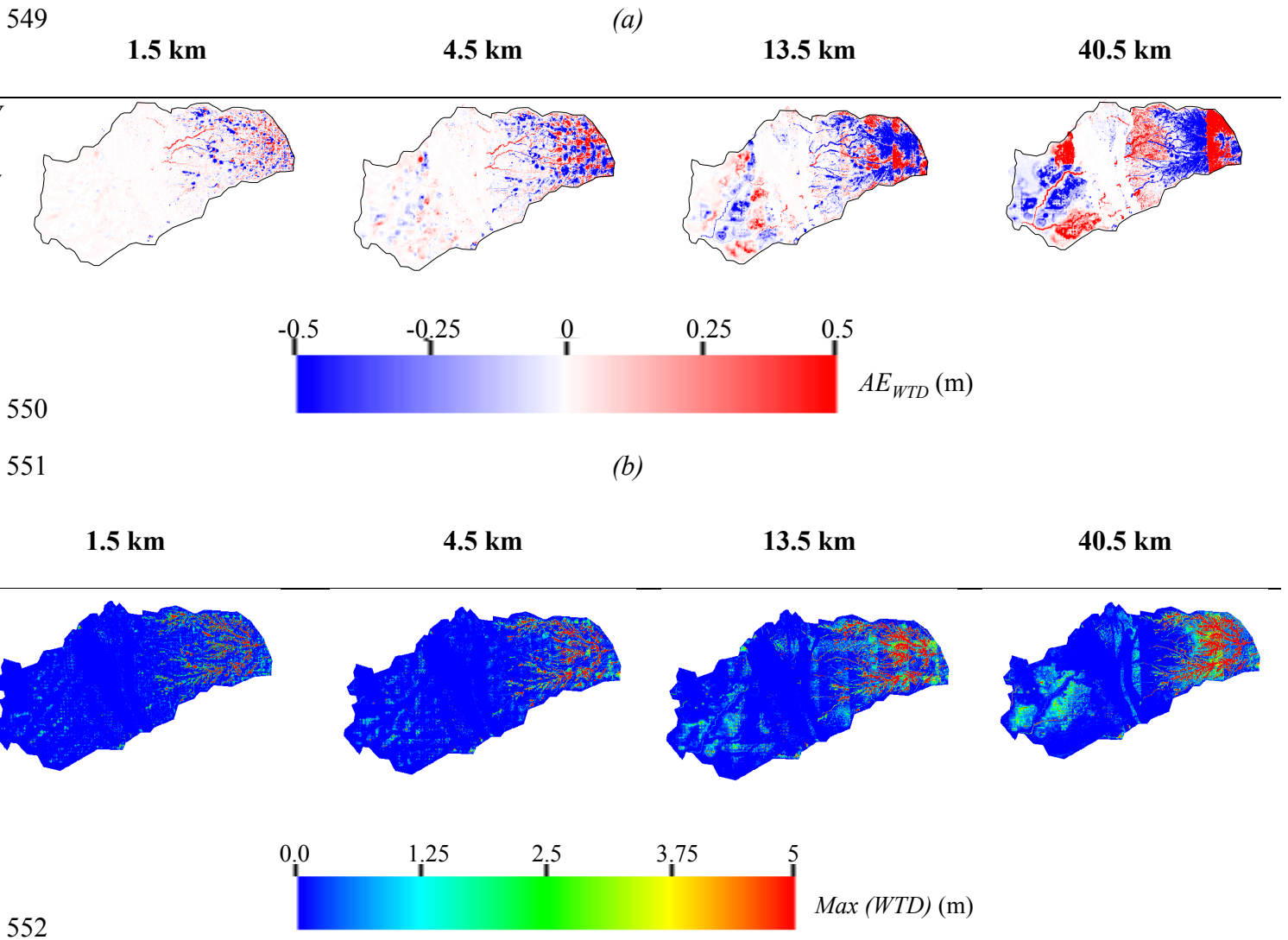
553     Figure 12: Spatial distributions of *(a)* the absolute error of Water Table Depth (WTD) ($AE_{WTD}$)

554     with respect to the highest spatial resolution of meteorological forcing (0.5 km) at WY day 333,

555     and *(b)* the max($AE_{WTD}$), with respect to the highest spatial resolution of meteorological forcing

556     (0.5 km).

557

558    Figure 12b depicts the maximum differences (for all time steps) of the water table depth

559    in absolute value between the results obtained with the highest spatial resolution and the other

560    four spatial resolutions. As previously stated, due to the almost zero permeability of the

561    intrusion, the latter is insensitive to the spatial resolution of the meteorological data. The water

562    table depth differences are as high as 5 m in several places, particularly in the Sierra Nevada

563    Mountains, following mostly trends in topography. In the Central Valley, noticeable differences

564    are mainly observed in the areas near the rivers and close to the pumping wells.

565    Figure 13 shows the temporal variations of the difference in the water table depth

566    between the highest resolution and the four other resolutions at 6 selected points. We selected

567    points located in the Central Valley as this zone hosts an alluvium aquifer (see their location in

568    Figure 1). For all these points, we note that the differences are almost zero for the spatial

569    resolution of 1.5 km indicating that this spatial resolution is sufficient to represent the

570    groundwater dynamics of this region. The spatial resolution of 4.5 km also shows relatively low

571    differences, the latter is indeed zero at three points and only points 2, 4 and 5 have non-zero

572    differences, but these remain less than 50 cm. The strongest differences are observed for results

573    obtained with forcing spatial resolutions of 13.5 and 40.5 km; note that the coarsest resolution

574    does not necessarily give the highest differences. In fact, at points 4 and 5, the highest

575    differences are obtained with the resolution of 13.5 km, indicative of the complex over- and

576    under- estimation patterns of bias observed at these coarser resolutions of forcing. In general, the

577    use of these large-scale spatial resolutions of forcing can lead to an over- or under -estimation of

578    the pressure-head between 50 cm and 10 m. Thus, while our results indicate that the spatial

579    resolution of meteorological forcing has little impact on the total groundwater storage, at discrete

580    points within the watershed the spatial resolution of forcing is very important, especially for

581 resolutions greater than 4.5 km. Again, this is particularly an issue for model calibration

582 purposes given that hydrologic numerical models are typically validated/calibrated by comparing

583 the groundwater measurements with the model outputs. In this case, our results indicate that

584 careful attention must be given to the spatial resolutions of forcing, as some errors are only due

585 to the latter not to any model parameterization.

586
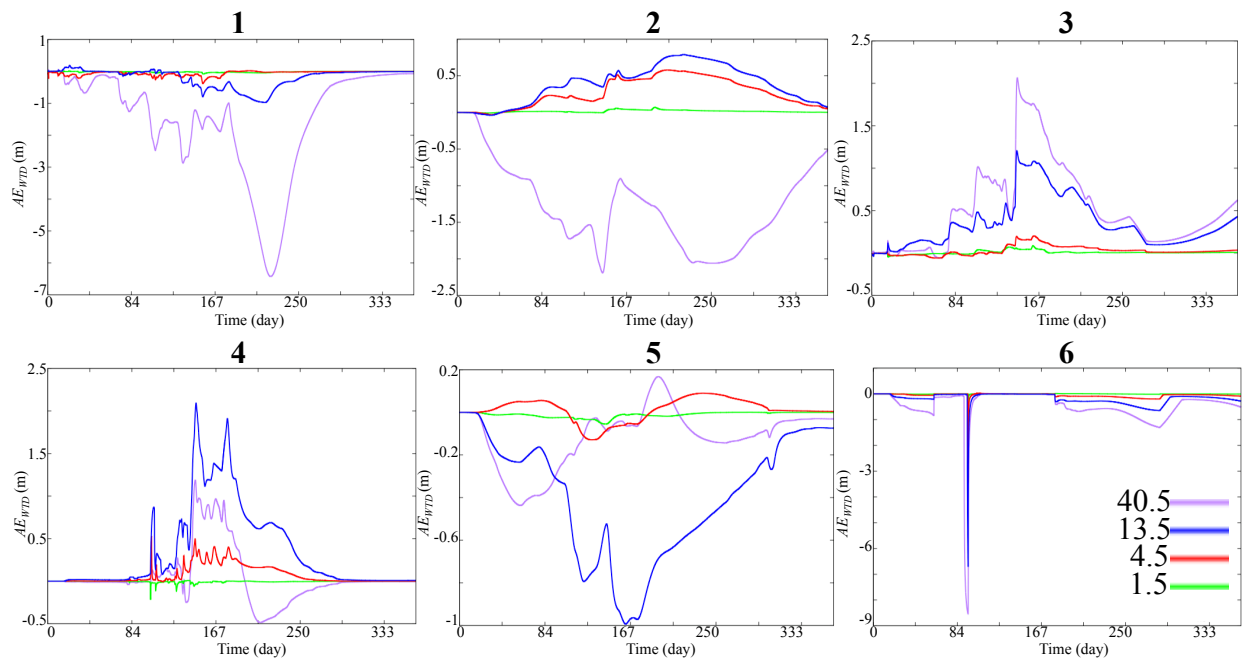
587

588 Figure 13: Absolute Error of the Water Table Depth ($AE_{WTD}$) with respect to the highest spatial

589 resolution of meteorological forcing (0.5 km) at six selected points.

590

591

## 5. Conclusions

593    Numerical methods that solve integrated hydrologic models are becoming increasingly

594 precise and spatially resolved. They thus require high-resolution and accurate input data such as

595 meteorological forcing. However, while integrated hydrologic models increase in precision, the

596    meteorological data used are most often of coarse resolution whereas these data are strongly

597    heterogeneous in space. It is, therefore, important to better understand not only how the

598    uncertainties associated with the spatial distribution of meteorological data affect hydrologic

599    model outputs, but also the meteorological forcing spatial resolution required to minimize these

600    uncertainties. Moreover, thanks to the advancement of atmospheric models, it is now possible to

601    obtain meteorological data closer to that of the resolution of hydrologic models.

602         In this study, we utilized the integrated hydrological model ParFlow-CLM to simulate the

603    hydrodynamics of a representative Californian watershed spanning the Sierra Nevada Mountains

604    and the Central Valley interface. The Cosumnes offers a unique opportunity to study semi-

605    natural flow conditions given its rare un-dammed river, one of the last in the state. Five different

606    spatial resolutions of meteorological data were obtained via the dynamical downscaling approach

607    of the Weather Research Forecasting (WRF) model. Both models were simulated in a high-

608    performance computing environment to accommodate the high spatio-temporal resolution of the

609    study. The Cosumnes watershed is characterized by strong variations of topography, geology,

610    land use and land cover leading to highly heterogeneous and complex atmospheric and

611    hydrologic dynamics, and is, therefore, an excellent candidate to better understand how the

612    different spatial resolutions of forcing affect the results of an integrated hydrologic model of a

613    watershed which include snow water equivalent, evapotranspiration, infiltration, surface and

614    groundwater levels.

615         Our results show that the impact of the spatial resolution of meteorological data depends

616    on the hydrologic component of interest, as well as the temporal and spatial scale.

617        • Snow accumulation and snowmelt are considerably impacted by forcing

618           resolution, even at the watershed scale. The results obtained with the different

619          spatial distributions suggest that meteorological data with a resolution close to the

620          one of the hydrologic model is needed to accurately reproduce the Snow Water

621          Equivalent (*SWE*) distribution as well as the total volume of *SWE*. Our results

622          show that the errors of *SWE* depend on both the spatial resolution of forcing and

623          topography and can be greater than 100 mm for a single point in time.

624      • At the watershed scale, global estimates of total evapotranspiration fluxes are

625          more or less insensitive to the spatial resolution of forcing. However, to obtain an

626          accurate spatial distribution of evapotranspiration which shows impacts of land

627          use, geology, and topography, higher resolutions of forcing are needed.

628      • The results obtained with infiltration are quite similar to those of

629          evapotranspiration. Note that for these two processes, the percent errors induce by

630          a coarser resolution are most often significant after a precipitation event, and that

631          these errors quickly subside once the precipitation ends.

632      • Forcing spatial resolution does not impact total surface water storage at the

633          watershed scale. Even for the coarsest resolution of forcing (40.5 km), the error,

634          increasing with time, is approximately 5%. However, we emphasize that for the

635          surface water levels at one point and at a given time, the differences between the

636          highest spatial resolution of the forcing data and the four other resolutions can

637          exceed 3 m. Regions within the Sierra Nevada Mountains are the most sensitive to

638          the spatial resolution of forcing data.

639      • Similar to surface water storage, the five different spatial resolutions of forcing

640          considered in this study led to similar groundwater storages. Therefore, the spatial

641          resolution of forcing has very small impacts on the hydrology simulated at a

642          watershed scale or hydrologic unit, hence non-grid based hydrologic models are

643          likely to be less sensitive to the spatial resolution of forcing than numerical

644          models. However, at a local scale, the variations of pressure head in the

645          subsurface obtained with the different resolutions can differ considerably, with

646          error as high as 9 m, especially in the Central Valley alluvium aquifers.

647          Groundwater level variations are the result of the aggregated impacts of land

648          surface processes. As such, the spatial resolutions of forcing affecting land

649          surface processes also impact groundwater levels. Our results show that these

650          impacts on groundwater are delayed in time due to the timing of the transfer of

651          water from the land surface to the subsurface.

652      Although the total water balance of the five spatial-resolutions of the meteorological

653    forcing is the same, the different spatial resolutions lead to different hydrological processes that

654    change both in time and space. For a good representation of the land surface processes

655    (infiltration, evapotranspiration and snow dynamics), a spatial resolution of the meteorological

656    data which is close to that of the hydrologic model is required due to the instantaneity and

657    complexities of these phenomena. For the surface and subsurface processes, we demonstrated

658    that for this watershed and those with similar characteristics, a spatial resolution of 4.5 km is

659    sufficient to reproduce the general physical trends of the hydrology. As a result, satellite-based

660    products such as NLDAS (with a resolution of around 14 km)  may induce errors that may limit

661    the use of their products if spatially accurate studies are needed. Because coarse spatial

662    resolutions of forcing may lead to very different groundwater and streamflow variations,

663    particular attention must be paid to the spatial resolution of meteorological data, especially in the

664    calibration and/or validation processes of numerical models. Indeed, the differences between the

665   measured and simulated hydrologic variables are not only due to the hydrodynamic parameters

666   of the model but may also be related to the parameterization of the meteorological data.

667   While in this study our focus is on the spatial distribution of meteorological data, future

668   studies will assess the propagation of uncertainties related to the temporal resolution of

669   meteorological forcing. Climate models are also used to predict the future weather conditions, it

670   would also be important to determine the ideal spatial-resolution of forcing in the context of a

671   warming climate. Because, Hydrologic Response Unit (HRU) based hydrologic models are also

672   commonly used, future work could further assess the sensitivity of these models to the spatial

673   distribution of meteorological data.

674

675

676   **Code and Data availability**

677   Simulations inputs, models and data are available from the authors upon request.

678

679

680

681

682

683 **Appendix A**

684       *A.1 Mass Balance Validation*

685 The physics represented for the four WRF domains are identical, except for cumulus

686 parameterization which is used for domains d01 (resolution of 13.5 km) and d02 (resolution of

687 13.5 km) and not for domains d03 (resolution of 1.5 km) and d04 (resolution of 0.5 km). This is

688 due to the fact that WRF can resolve convection explicitly at resolutions higher than around 4 km

689 (Gilliland and Rowe, 2007). To assess the sensitiviy of the WRF simulated forcings to this

690 inevitable incosistancy between the domains, we compare watershed-wide daily precipitation

691 and air tempeature in Figure A1. Our results show that there are minimal differences (RMSE of

692 less than 0.002 m and 0.01°C for precipitation and temperature, respcetivly) between the four

693 WRF domains, when averaged over the watershed. This shows that the only difference between

694 the forcings from WRF domains are due to different resolutions and the effects of described

695 difference in physics representations are limited.
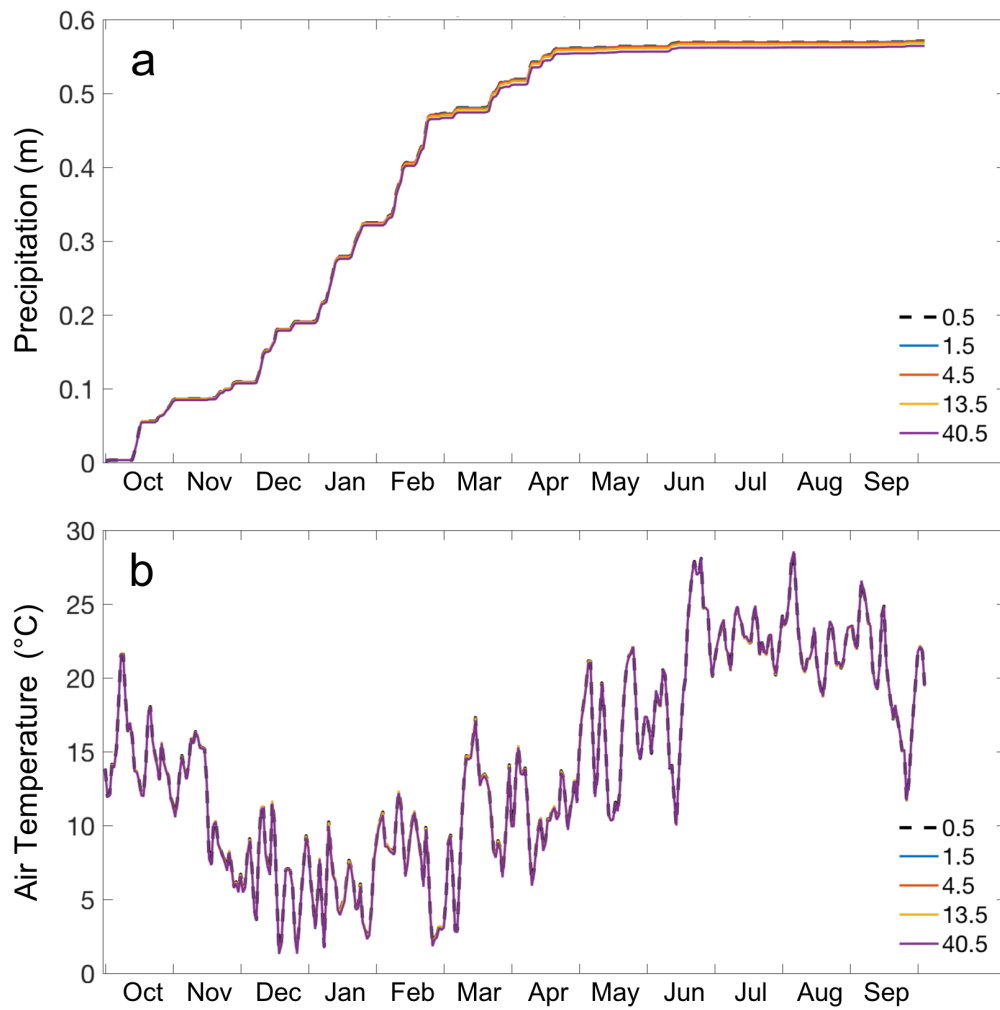
696

697    Figure A1: Daily variations of WRF simulated precipitation (a) and air temperature (b), averaged

698    over the entire watershed for spatial resolutions of 0.5, 1.5, 4.5, 13.5, and 40.5 km.

699

 *A.2 Spatial distributions of precipitation and temperature over the domain d04*
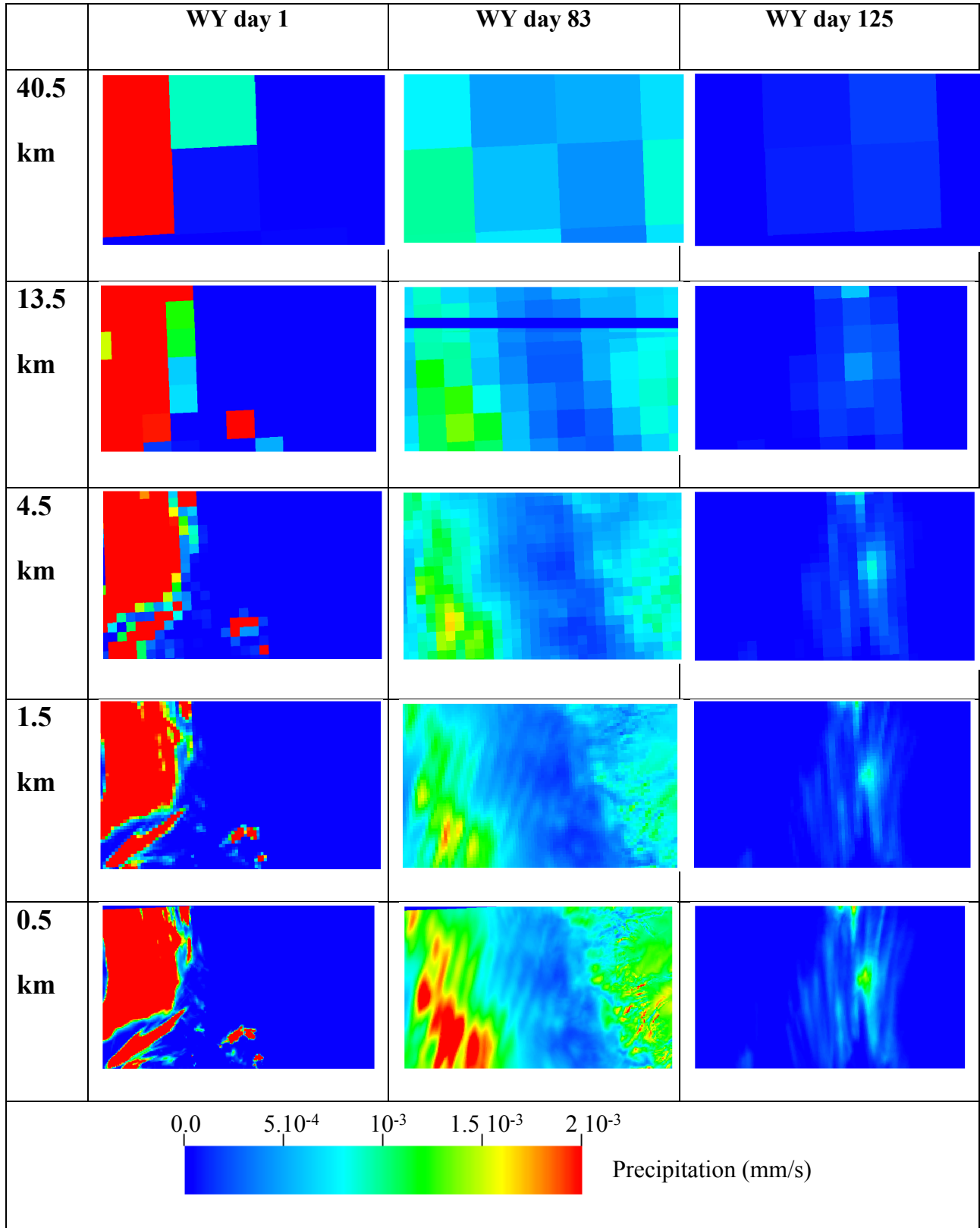
701 Figure A2: Spatial distributions of precipitation associated with the five spatial resolutions of

702 meteorological at three selected times corresponding to periods where the storm has high (day 1)

703 and low (day 83) intensity and a time a very located and low intensity (day 125).

704
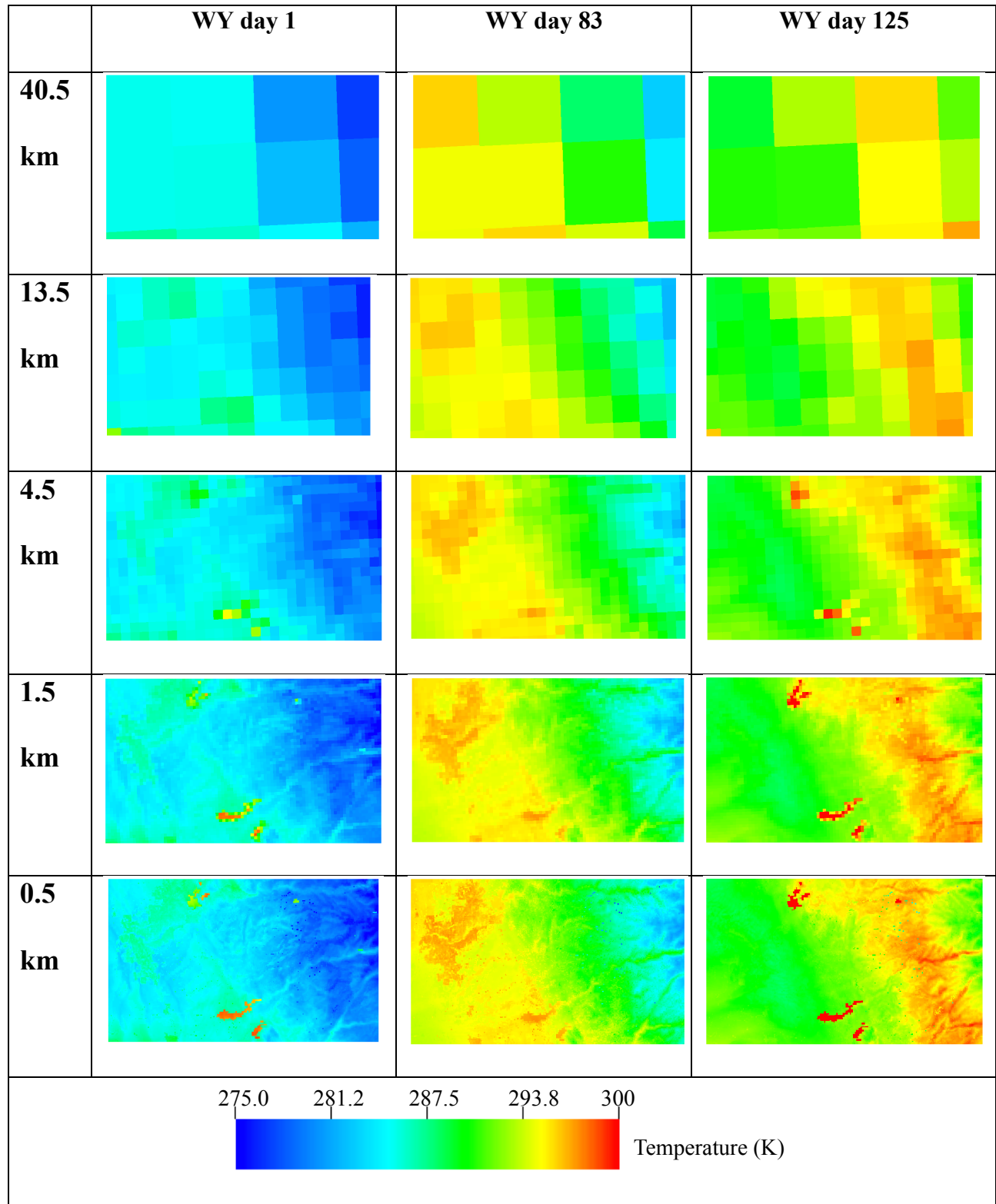
706 Figure A3: Spatial distributions of temperature associated with the five spatial resolutions of

707 meteorological at three selected times corresponding to periods where the storm has high (day 1)

708 and low (day 83) intensity and a time a very located and low intensity (day 125).

709

710

711   *A.3 Comparisons with ground measurements*

712        We compared simulated precipitation and temperature with ground measurements. We

713   selected four stations, which continuously measure precipitation and temperature. The Figure

714   below shows the location of these stations as well as the comparisons. We only show

715   comparisons with the results obtained with the highest resolution (i.e. d04) for graphical

716   purposes.
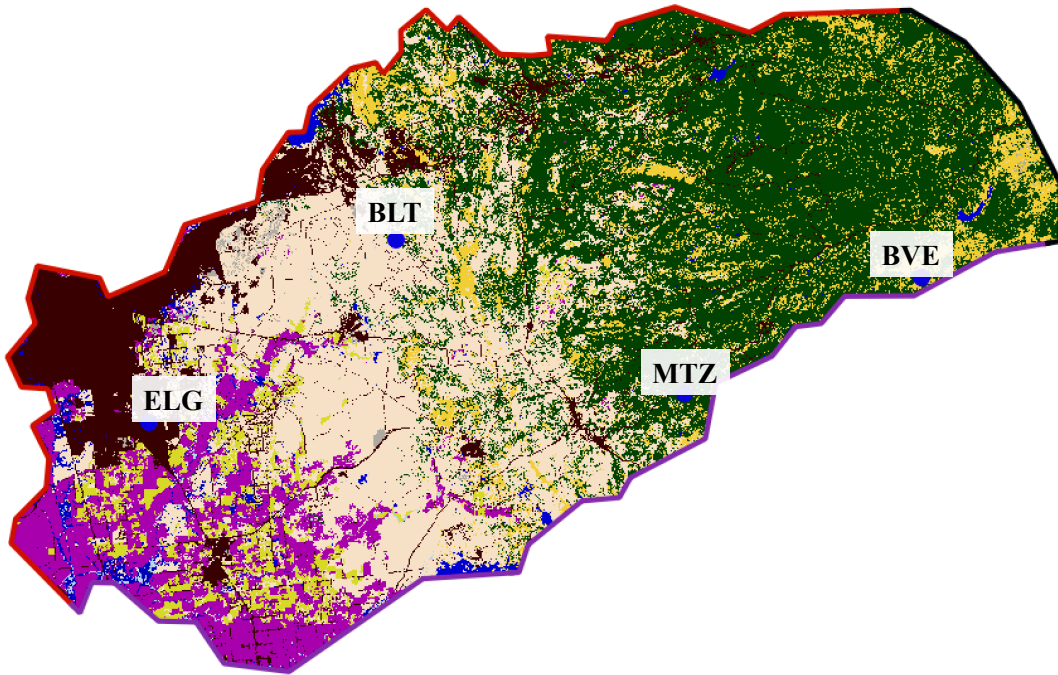
717

718   Figure A4a: location of the four selected stations. These stations allow comparing the simulated

719   precipitation and temperature with measurements in the Sierra Nevada mountains (BVE and

720   MTZ), the volcanic intrusion (BLT), and the Central Valley (ELG).

721

722
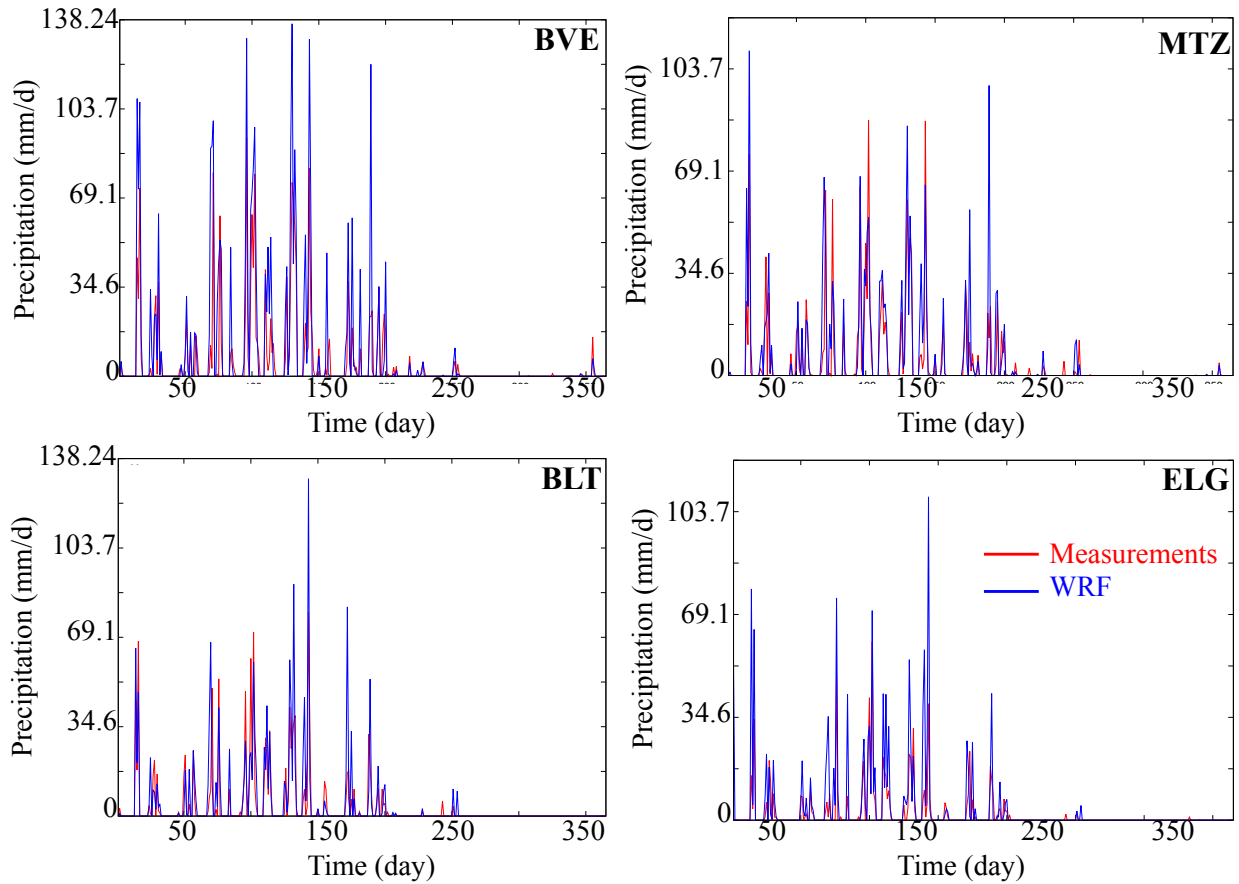
723

724 Figure A4b: Comparisons between simulated and measured precipitation at the four selected

725 stations. The reasonable match between measurements and simulations at different locations

726 allows gaining confidence in the WRF simulations to reproduce the atmospheric dynamics at

727 different elevations
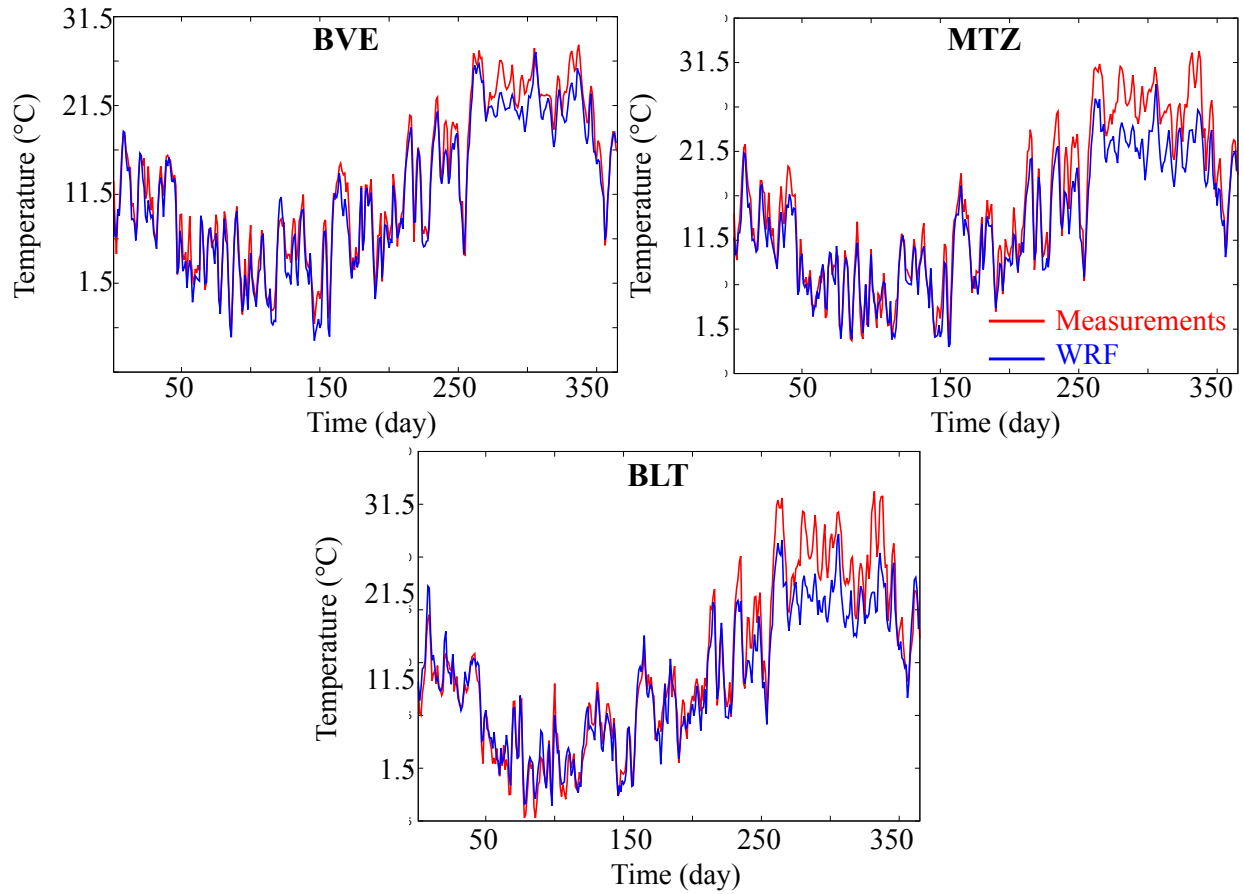
728

729    Figure A4c: Comparisons between the simulated and measured temperature at three selected

730    stations. The station ELG does not have measurements of temperature. Like the precipitations

731    results, our comparisons indicate a reasonable match between measurements and simulations.

732

733

**Author contribution**

734 The authors contribute equally to this work.

735

736

**Competing interests**

737 The authors declare that they have no conflict of interest.

738

739

**Acknowledgements**

740 This work was supported by http://dx.doi.org/10.13039/ 100007000 (LDRD) funding from
741 Berkeley Lab, provided by the Director, Office of Science, of the U.S. Department of Energy
742 under Contract No. DE-AC02-05CH11231. This research used computing resources from the
743 National Energy Research Scientific Computing Center, a DOE Office of Science User Facility
744 supported by the http:// dx.doi.org/10.13039/100006132 of the U.S. Department of Energy under
745 Contract No. DE-AC02-05CH11231.

746 The authors are thankful to Peter-James Dennedy-Frank for his careful reading and constructive
747 suggestions and comments.

749 **References**

750 Abbott, M. B., Bathurst, J. C., Cunge, J. A., O'Connell, P. E. and Rasmussen, J.: An introduction
751 to the European Hydrological System — Systeme Hydrologique Europeen, "SHE", 2: Structure
752 of a physically-based, distributed modelling system, Journal of Hydrology, 87(1), 61–77,
753 doi:10.1016/0022-1694(86)90115-0, 1986.

754 Arnaud, P., Bouvier, C., Cisneros, L. and Dominguez, R.: Influence of rainfall spatial variability
755 on flood prediction, Journal of Hydrology, 260(1), 216–230, doi:10.1016/S0022-1694(01)00611-
756 4, 2002.

757 Belfort, B., Ramasomanana, F., Younes, A. and Lehmann, F.: An Efficient Lumped Mixed
758 Hybrid Finite Element Formulation for Variably Saturated Groundwater Flow, Vadose Zone
759 Journal, 8(2), 352–362, doi:10.2136/vzj2008.0108, 2009.

760 Bergamaschi, L. and Putti, M.: Mixed Finite Elements and Newton-Type Linearizations for the
761 Solution of Richards' Equation., n.d.

762 Berne, A., Delrieu, G., Creutin, J.-D. and Obled, C.: Temporal and spatial resolution of rainfall
763 measurements required for urban hydrology, Journal of Hydrology, 299(3), 166–179,
764 doi:10.1016/j.jhydrol.2004.08.002, 2004.

765 Beven, K.: Prophecy, reality and uncertainty in distributed hydrological modelling, Advances in
766 Water Resources, 16(1), 41–51, doi:10.1016/0309-1708(93)90028-E, 1993.

767 Beven, K. and Binley, A.: The future of distributed models: Model calibration and uncertainty
768 prediction, Hydrological Processes, 6(3), 279–298, doi:10.1002/hyp.3360060305, 1992.

769 Boryan, C., Yang, Z., Mueller, R. and Craig, M.: Monitoring US agriculture: the US Department
770 of Agriculture, National Agricultural Statistics Service, Cropland Data Layer Program, Geocarto
771 International, 26(5), 341–358, doi:10.1080/10106049.2011.562309, 2011.

772 Bretherton, C. S. and Park, S.: A New Moist Turbulence Parameterization in the Community
773 Atmosphere Model, J. Climate, 22(12), 3422–3448, doi:10.1175/2008JCLI2556.1, 2009.

774 Cosgrove, B. A., Lohmann, D., Mitchell, K. E., Houser, P. R., Wood, E. F., Schaake, J. C.,
775 Robock, A., Marshall, C., Sheffield, J., Duan, Q., Luo, L., Higgins, R. W., Pinker, R. T., Tarpley,
776 J. D. and Meng, J.: Real-time and retrospective forcing in the North American Land Data
777 Assimilation System (NLDAS) project, Journal of Geophysical Research: Atmospheres,
778 108(D22), doi:10.1029/2002JD003118, 2003.

779 Dai, Y., Zeng, X., Dickinson, R. E., Baker, I., Bonan, G. B., Bosilovich, M. G., Denning, A. S.,
780 Dirmeyer, P. A., Houser, P. R., Niu, G., Oleson, K. W., Schlosser, C. A. and Yang, Z.-L.: The
781 Common Land Model, Bull. Amer. Meteor. Soc., 84(8), 1013–1024, doi:10.1175/BAMS-84-8-
782 1013, 2003.

783 Dankers, R., Christensen, O. B., Feyen, L., Kalas, M. and de Roo, A.: Evaluation of very high-
784 resolution climate model data for simulating flood hazards in the Upper Danube Basin, Journal
785 of Hydrology, 347(3), 319–331, doi:10.1016/j.jhydrol.2007.09.055, 2007.

786 Dettinger, M.: Climate Change, Atmospheric Rivers, and Floods in California – A Multimodel
787 Analysis of Storm Frequency and Magnitude Changes1, JAWRA Journal of the American Water
788 Resources Association, 47(3), 514–523, doi:10.1111/j.1752-1688.2011.00546.x, 2011.

789 Dettinger, M. and Anderson, M. L.: Storage in California's reservoirs and snowpack in this time
790 of drought, San Francisco Estuary and Watershed Science, 13(2),
791 doi:10.15447/sfews.2015v13iss2art1, 2015.

792 Di Liberto, T.: Very wet 2017 water year ends in California, NOAA Climate.gov [online]
793 Available from: https://www.climate.gov/news-features/featured-images/very-wet-2017-water-
794 year-ends-california (Accessed 18 October 2018), 2017.

795 Dudhia, J.: Numerical Study of Convection Observed during the Winter Monsoon Experiment
796 Using a Mesoscale Two-Dimensional Model, J. Atmos. Sci., 46(20), 3077–3107,
797 doi:10.1175/1520-0469(1989)046<3077:NSOCOD>2.0.CO;2, 1988.

798 Elsner, M. M., Gangopadhyay, S., Pruitt, T., Brekke, L. D., Mizukami, N. and Clark, M. P.: How
799 Does the Choice of Distributed Meteorological Data Affect Hydrologic Model Calibration and
800 Streamflow Simulations?, J. Hydrometeor., 15(4), 1384–1403, doi:10.1175/JHM-D-13-083.1,
801 2014.

802 Eum, H.-I., Dibike, Y., Prowse, T. and Bonsal, B.: Inter-comparison of high-resolution gridded
803 climate data sets and their implication on hydrological model simulation over the Athabasca
804 Watershed, Canada, Hydrological Processes, 28(14), 4250–4271, doi:10.1002/hyp.10236, 2014.

805 Fahs, M., Younes, A. and Lehmann, F.: An easy and efficient combination of the Mixed Finite
806 Element Method and the Method of Lines for the resolution of Richards' Equation,
807 Environmental Modelling & Software, 24(9), 1122–1126, doi:10.1016/j.envsoft.2009.02.010,
808 2009.

809 Faunt, C. C. and Geological Survey (U.S.), Eds.: Groundwater availability of the Central Valley
810 Aquifer, California, U.S. Geological Survey, Reston, Va., 2009.

811 Faunt, C. C., Belitz, K. and Hanson, R. T.: Development of a three-dimensional model of
812 sedimentary texture in valley-fill deposits of Central Valley, California, USA, Hydrogeology
813 Journal, 18(3), 625–649, doi:10.1007/s10040-009-0539-7, 2010.

814 Flint, L. E., Flint, A. L., Thorne, J. H. and Boynton, R.: Fine-scale hydrologic modeling for
815 regional landscape applications: the California Basin Characterization Model development and
816 performance, Ecological Processes, 2(1), 25, doi:10.1186/2192-1709-2-25, 2013.

817 Fu, S., Sonnenborg, T. O., Jensen, K. H. and He, X.: Impact of Precipitation Spatial Resolution
818 on the Hydrological Response of an Integrated Distributed Water Resources ModelAll rights

819  reserved. No part of this periodical may be reproduced or transmitted in any form or by any
820  means, electronic or mechanical, including photocopying, recording, or any information storage
821  and retrieval system, without permission in writing from the publisher., Vadose Zone Journal,
822  10(1), 25–36, doi:10.2136/vzj2009.0186, 2011.

823  van Genuchten, M. T.: A Closed-form Equation for Predicting the Hydraulic Conductivity of
824  Unsaturated  Soils1,  Soil  Science  Society  of  America  Journal,  44(5),  892,
825  doi:10.2136/sssaj1980.03615995004400050002x, 1980.

826  Geologic Map of California: Geologic Map of California, Geologic Map of California [online]
827  Available from: https://maps.conservation.ca.gov/cgs/gmc/ (Accessed 17 October 2018), 2015.

828  Gilbert, J. M. and Maxwell, R. M.: Examining regional groundwater–surface water
829  dynamics using an integrated hydrologic model of the San Joaquin River basin, Hydrology and
830  Earth System Sciences, 21(2), 923–947, doi:https://doi.org/10.5194/hess-21-923-2017, 2017.

831  Gilbert, J. M., Jefferson, J. L., Constantine, P. G. and Maxwell, R. M.: Global spatial sensitivity
832  of runoff to subsurface permeability using the active subspace method, Advances in Water
833  Resources, 92, 30–42, doi:10.1016/j.advwatres.2016.03.020, 2016.

834  Gilliland, E. and Rowe, C.: A comparison of cumulus parameterizationschemes in the WRF
835  model, in Proceedings of the 87th AMS AnnualMeeting & 21th Conference on Hydrology, pp:
836  2.16.  [online]  Available  from:
837  https://www.google.com/search?q=A+comparison+of+cumulus+parameterizationschemes+in+th
838  e+WRF+model&oq=A+comparison+of+cumulus+parameterizationschemes+in+the+WRF+mod
839  el&aqs=chrome..69i57j0.434j0j7&sourceid=chrome&ie=UTF-8 (Accessed 16 August 2019),
840  2007.

841  Grell, G. A. and Freitas, S. R.: A scale and aerosol aware stochastic convective parameterization
842  for weather and air quality modeling, Atmospheric Chemistry and Physics, 14(10), 5233–5250,
843  doi:https://doi.org/10.5194/acp-14-5233-2014, 2014.

844  Griffin, D. and Anchukaitis, K. J.: How unusual is the 2012–2014 California drought?,
845  Geophysical Research Letters, 41(24), 9017–9023, doi:10.1002/2014GL062433, 2014.

846  Haddeland, I., Lettenmaier, D. P. and Skaugen, T.: Effects of irrigation on the water and energy
847  balances of the Colorado and Mekong river basins, Journal of Hydrology, 324(1), 210–223,
848  doi:10.1016/j.jhydrol.2005.09.028, 2006.

849  Hassane Maina, F. and Ackerer, P.: Ross scheme, Newton–Raphson iterative methods and time-
850  stepping strategies for solving the mixed form of Richards' equation, Hydrol. Earth Syst. Sci.,
851  21(6), 2667–2683, doi:10.5194/hess-21-2667-2017, 2017.

852  Homer, C., Dewitz, J., Yang, L., Jin, S., Danielson, P., Xian, G., Coulston, J., Herold, N.,
853  Wickham, J. and Megown, K.: Completion of the 2011 National Land Cover Database for the
854  conterminous United States–representing a decade of land cover change information,
855  Photogrammetric Engineering & Remote Sensing, 81(5), 345–354, 2015.

IGBP: Global plant database published - IGBP, [online] Available from: http://www.igbp.net/news/news/news/globalplantdatabasepublished.5.1b8ae20512db692f2a6800 014762.html (Accessed 18 October 2018), 2018.

Janetti, E. B., Guadagnini, L., Riva, M. and Guadagnini, A.: Global sensitivity analyses of multiple conceptual models with uncertain parameters driving groundwater flow in a regional-scale sedimentary aquifer, Journal of Hydrology, doi:10.1016/j.jhydrol.2019.04.035, 2019.

Jennings, C. W., Strand, R. G. and Rogers, T. H.: Geologic map of California, 1977.

Kleinn, J., Frei, C., Gurtz, J., Lüthi, D., Vidale, P. L. and Schär, C.: Hydrologic simulations in the Rhine basin driven by a regional climate model, Journal of Geophysical Research: Atmospheres, 110(D4), doi:10.1029/2004JD005143, 2005.

Kollet, S. J. and Maxwell, R. M.: Integrated surface–groundwater flow modeling: A free-surface overland flow boundary condition in a parallel groundwater flow model, Advances in Water Resources, 29(7), 945–958, doi:10.1016/j.advwatres.2005.08.006, 2006.

Koren, V. I., Finnerty, B. D., Schaake, J. C., Smith, M. B., Seo, D.-J. and Duan, Q.-Y.: Scale dependencies of hydrologic models to spatial variability of precipitation, Journal of Hydrology, 217(3), 285–302, doi:10.1016/S0022-1694(98)00231-5, 1999.

Liu, Y. and Gupta, H. V.: Uncertainty in hydrologic modeling: Toward an integrated data assimilation framework, Water Resources Research, 43(7), doi:10.1029/2006WR005756, 2007.

Lobligeois, F., Andréassian, V., Perrin, C., Tabary, P. and Loumagne, C.: When does higher spatial resolution rainfall information improve streamflow simulation? An evaluation using 3620 flood events, Hydrology and Earth System Sciences, 18(2), 575–594, doi:https://doi.org/10.5194/hess-18-575-2014, 2014.

Maina, F. Z. and Guadagnini, A.: Uncertainty Quantification and Global Sensitivity Analysis of Subsurface Flow Parameters to Gravimetric Variations During Pumping Tests in Unconfined Aquifers, Water Resour. Res., 54(1), 501–518, doi:10.1002/2017WR021655, 2018.

Maina, F. Z. and Siirila-Woodburn, E. R.: Watersheds dynamics following wildfires: nonlinear feedbacks and implications on hydrologic responses, Hydrological Processes, 0(ja), doi:10.1002/hyp.13568, 2019.

Maina, F. Z. and Siirila-Woodburn, E. R.: Watersheds dynamics following wildfires: Nonlinear feedbacks and implications on hydrologic responses, Hydrological Processes, 34(1), 33–50, doi:10.1002/hyp.13568, 2020.

Maina, F. Z., Siirila-Woodburn, E. R., Newcomer, M., Xu, Z. and Steefel, C.: Determining the impact of a severe dry to wet transition on watershed hydrodynamics in California, USA with an integrated hydrologic model, Journal of Hydrology, 580, 124358, doi:10.1016/j.jhydrol.2019.124358, 2020.

891 Maxwell, R. M.: A terrain-following grid transform and preconditioner for parallel, large-scale,
892 integrated hydrologic modeling, Advances in Water Resources, 53, 109–117,
893 doi:10.1016/j.advwatres.2012.10.001, 2013.

894 Maxwell, R. M. and Miller, N. L.: Development of a Coupled Land Surface and Groundwater
895 Model, Journal of Hydrometeorology, 6(3), 233–247, doi:10.1175/JHM422.1, 2005.

896 Mendoza, P. A., Mizukami, N., Ikeda, K., Clark, M. P., Gutmann, E. D., Arnold, J. R., Brekke,
897 L. D. and Rajagopalan, B.: Effects of different regional climate model resolution and forcing
898 scales on projected hydrologic changes, Journal of Hydrology, 541, 1003–1019,
899 doi:10.1016/j.jhydrol.2016.08.010, 2016.

900 Miller, C. T., Williams, G. A., Kelley, C. T. and Tocci, M. D.: Robust solution of Richards'
901 equation for nonuniform porous media, Water Resour. Res., 34(10), 2599–2610,
902 doi:10.1029/98WR01673, 1998.

903 Mlawer, E. J., Taubman, S. J., Brown, P. D., Iacono, M. J. and Clough, S. A.: Radiative transfer
904 for inhomogeneous atmospheres: RRTM, a validated correlated-k model for the longwave,
905 Journal of Geophysical Research: Atmospheres, 102(D14), 16663–16682,
906 doi:10.1029/97JD00237, 1997.

907 Monin, A. S. and Obukhov, A. M.: Basic laws of turbulent mixing in the surface layer of the
908 atmosphere, Contributions of the Geophysical Institute of the Slovak Academy of Sciences, vol.
909 24, no. 151, pp. 163–187 [online] Available from: http://www.oalib.com/references/13491049
910 (Accessed 6 August 2019), 1954.

911 Morrison, H., Thompson, G. and Tatarskii, V.: Impact of Cloud Microphysics on the
912 Development of Trailing Stratiform Precipitation in a Simulated Squall Line: Comparison of
913 One- and Two-Moment Schemes, Mon. Wea. Rev., 137(3), 991–1007,
914 doi:10.1175/2008MWR2556.1, 2009.

915 Nicótina, L., Celegon, E. A., Rinaldo, A. and Marani, M.: On the impact of rainfall patterns on
916 the hydrologic response, Water Resources Research, 44(12), doi:10.1029/2007WR006654, 2008.

917 Ochoa-Rodriguez, S., Wang, L.-P., Gires, A., Pina, R. D., Reinoso-Rondinel, R., Bruni, G.,
918 Ichiba, A., Gaitan, S., Cristiano, E., van Assel, J., Kroll, S., Murlà-Tuyls, D., Tisserand, B.,
919 Schertzer, D., Tchiguirinskaia, I., Onof, C., Willems, P. and ten Veldhuis, M.-C.: Impact of
920 spatial and temporal resolution of rainfall inputs on urban hydrodynamic modelling outputs: A
921 multi-catchment investigation, Journal of Hydrology, 531, 389–407,
922 doi:10.1016/j.jhydrol.2015.05.035, 2015.

923 Olsson, J., Berg, P. and Kawamura, A.: Impact of RCM Spatial Resolution on the Reproduction
924 of Local, Subdaily Precipitation, J. Hydrometeor., 16(2), 534–547, doi:10.1175/JHM-D-14-
925 0007.1, 2014.

926    Panday, S. and Huyakorn, P. S.: A fully coupled physically-based spatially-distributed model for
927    evaluating surface/subsurface flow, Advances in Water Resources, 27(4), 361–382,
928    doi:10.1016/j.advwatres.2004.02.016, 2004.

929    Prein, A. F., Holland, G. J., Rasmussen, R. M., Done, J., Ikeda, K., Clark, M. P. and Liu, C. H.:
930    Importance of Regional Climate Model Grid Spacing for the Simulation of Heavy Precipitation
931    in the Colorado Headwaters, J. Climate, 26(13), 4848–4857, doi:10.1175/JCLI-D-12-00727.1,
932    2013.

933    Rasmussen, R., Liu, C., Ikeda, K., Gochis, D., Yates, D., Chen, F., Tewari, M., Barlage, M.,
934    Dudhia, J., Yu, W., Miller, K., Arsenault, K., Grubišić, V., Thompson, G. and Gutmann, E.:
935    High-Resolution Coupled Climate Runoff Simulations of Seasonal Snowfall over Colorado: A
936    Process Study of Current and Warmer Climate, J. Climate, 24(12), 3015–3048,
937    doi:10.1175/2010JCLI3985.1, 2011.

938    Richards, L. A.: Capillary conduction of liquids through porous medium, Journal of Applied
939    Physics, 1(5), 318–333, doi:10.1063/1.1745010, 1931.

940    Schilling, W.: Rainfall data for urban hydrology: what do we need?, Atmospheric Research,
941    27(1), 5–21, doi:10.1016/0169-8095(91)90003-F, 1991.

942    SCRIPPS Institution of Oceanograohy: Northern California Just Surpassed the Wettest Year on
943    Record | Scripps Institution of Oceanography, UC San Diego, [online] Available from:
944    https://scripps.ucsd.edu/news/northern-california-just-surpassed-wettest-year-record (Accessed
945    18 October 2018), 2017.

946    Shrestha, R., Tachikawa, Y. and Takara, K.: Input data resolution analysis for distributed
947    hydrological modeling, Journal of Hydrology, 319(1), 36–50, doi:10.1016/j.jhydrol.2005.04.025,
948    2006.

949    Skamarock, C., Klemp, B., Dudhia, J., Gill, O., Barker, D., Duda, G., Huang, X., Wang, W. and
950    Powers, G.: A Description of the Advanced Research WRF Version 3, ,
951    doi:10.5065/D68S4MVH, 2008a.

952    Skamarock, C., Klemp, B., Dudhia, J., Gill, O., Barker, D., Duda, G., Huang, X., Wang, W. and
953    Powers, G.: A Description of the Advanced Research WRF Version 3, ,
954    doi:10.5065/D68S4MVH, 2008b.

955    Skamarock, W. C. and Klemp, J. B.: A Time-split Nonhydrostatic Atmospheric Model for
956    Weather Research and Forecasting Applications, J. Comput. Phys., 227(7), 3465–3485,
957    doi:10.1016/j.jcp.2007.01.037, 2008.

958    Srivastava, V., Graham, W., Muñoz-Carpena, R. and Maxwell, R. M.: Insights on geologic and
959    vegetative controls over hydrologic behavior of a large complex basin – Global Sensitivity
960    Analysis of an integrated parallel hydrologic model, Journal of Hydrology, 519, 2238–2257,
961    doi:10.1016/j.jhydrol.2014.10.020, 2014.

962 Swain, D. L., Langenbrunner, B., Neelin, J. D. and Hall, A.: Increasing precipitation volatility in
963 twenty-first-century California, Nature Clim Change, 8(5), 427–433, doi:10.1038/s41558-018-
964 0140-y, 2018.

965 Tobin, C., Nicotina, L., Parlange, M. B., Berne, A. and Rinaldo, A.: Improved interpolation of
966 meteorological forcings for hydrologic applications in a Swiss Alpine region, Journal of
967 Hydrology, 401(1), 77–89, doi:10.1016/j.jhydrol.2011.02.010, 2011.

968 Tocci, M. D., Kelley, C. T. and Miller, C. T.: Accurate and economical solution of the pressure-
969 head form of Richards' equation by the method of lines, Advances in Water Resources, 20(1), 1–
970 14, doi:10.1016/S0309-1708(96)00008-5, 1997.

971 Vahmani, P. and Jones, A. D.: Water conservation benefits of urban heat mitigation, Nat
972 Commun, 8(1), 1–9, doi:10.1038/s41467-017-01346-1, 2017.

973 Vahmani, P., Jones, A. and Patricola, C. M.: Interacting implications of climate change,
974 population dynamics, and urban heat mitigation for future exposure to heat extremes, Environ.
975 Res. Lett., doi:10.1088/1748-9326/ab28b0, 2019.

976 Vergara, H., Hong, Y., Gourley, J. J., Anagnostou, E. N., Maggioni, V., Stampoulis, D. and
977 Kirstetter, P.-E.: Effects of Resolution of Satellite-Based Rainfall Estimates on Hydrologic
978 Modeling Skill at Different Scales, J. Hydrometeor., 15(2), 593–613, doi:10.1175/JHM-D-12-
979 0113.1, 2013.

980 Welch, L. A. and Allen, D. M.: Hydraulic conductivity characteristics in mountains and
981 implications for conceptualizing bedrock groundwater flow, Hydrogeol J, 22(5), 1003–1026,
982 doi:10.1007/s10040-014-1121-5, 2014.

983